The role of viscous heating in Barrovian metamorphism of collisional orogens: thermomechanical models and application to the Lepontine Dome in the Central Alps

J.-P. BURG[1] AND T. V. GERYA[1,2]
[1]*Geologisches Institut - ETH - Zürich, CH-8092 Zurich, Switzerland (jean-pierre.burg@erdw.ethz.ch)*
[2]*Institute of Experimental Mineralogy, Russian Academy of Sciences, 142432 Chernogolovka, Moscow, Russia*

ABSTRACT Thermal models for Barrovian metamorphism driven by doubling the thickness of the radiogenic crust typically meet difficulty in accounting for the observed peak metamorphic temperature conditions. This difficulty suggests that there is an additional component in the thermal budget of many collisional orogens. Theoretical and geological considerations suggest that viscous heating is a cumulative process that may explain the heat deficit in collision orogens. The results of 2D numerical modelling of continental collision involving subduction of the lithospheric mantle demonstrate that geologically plausible stresses and strain rates may result in orogen-scale viscous heat production of 0.1 to $>1\ \mu$W m^{-3}, which is comparable to or even exceeds bulk radiogenic heat production within the crust. Thermally induced buoyancy is responsible for crustal upwelling in large domes with metamorphic temperatures up to 200 °C higher than regional background temperatures. Heat is mostly generated within the uppermost mantle, because of large stresses in the highly viscous rocks deforming there. This thermal energy may be transferred to the overlying crust either in the form of enhanced heat flow, or through magmatism that brings heat into the crust advectively. The amplitude of orogenic heating varies with time, with both the amplitude and time-span depending strongly on the coupling between heat production, viscosity and collision strain rate. It is argued that geologically relevant figures are applicable to metamorphic domes such as the Lepontine Dome in the Central Alps. We conclude that deformation-generated viscous dissipation is an important heat source during collisional orogeny and that high metamorphic temperatures as in Barrovian type metamorphism are inherent to deforming crustal regions.

Keywords: Alps; Barrovian metamorphism; Lepontine Dome; numerical modelling; viscous heating.

INTRODUCTION

Intermediate-pressure (Barrovian) metamorphism is a long-known, first-order feature that typifies many ancient and nearly all modern orogenic regions in collision settings (e.g. Miyashiro, 1973; Winter, 2001). However, the pressure–temperature–time evolution of Barrovian rocks remains difficult to explain (e.g. Thompson & Ridley, 1987). 'Barrovian metamorphism: where's the heat?' asked Jamieson *et al.* (1998). Whereas viscous heating is undeniable for high strain, preservation of tectonic overpressures in mineral assemblages is not established (even though overpressures may well occur in a rock's history). A number of thermo-mechanical models demonstrated that nappe stacking of heat-producing, radioactive continental crust usually fails to provide the amount of heat needed to attain the peak metamorphic temperatures commonly obtained from thermobarometric calculations (e.g. Jamieson *et al.*, 1998; Engi *et al.*, 2001). An answer is to assume that orogens have formed where materials with especially high radioactive heat production existed before orogeny (e.g. Chamberlain & Sonder, 1990; Huerta *et al.*, 1998; Goffé *et al.*, 2003). However, the thermal equilibration time remains typically too slow with respect to independent geochronological constraints on the timing of thrusting and the subsequent thermal peak of metamorphism. Such considerations point towards the significant bulk effects of viscous heating during orogeny. A common weakness of most thermo-mechanical modelling of convergent orogenic wedges (e.g. Allemand & Lardeaux, 1997; Beaumont *et al.*, 2001; Burov *et al.*, 2001; Doin & Henry, 2001; Jamieson *et al.*, 2002; Pysklywec *et al.*, 2002) is that the heat derived from mechanical work is neglected: a recent exception is Babeyko *et al.* (2002). It is argued that first, in a deforming orogen, viscous heating actually is an *in situ* physical mechanism potentially capable of accounting for the thermal budget shortfall on the appropriate timescale. Two-dimensional (2D) numerical experiments are presented that incorporate viscous heating in modelling collision orogens. We argue that these results are applicable to classical examples of *P–T–t* paths such as in the Central Alps, without the need for anomalously high heat production in the crust.

VISCOUS HEATING: PHYSICAL PRINCIPLES AND GEOLOGICAL CONSIDERATIONS

Several authors (e.g. Graham & England, 1976; England & Thompson, 1984; Molnar & England, 1990; Genser *et al.*, 1996; Kincaid & Silver, 1996) have advocated frictional heating, also termed viscous dissipation, as a significant contributor to the heat budget of metamorphism. The magnitude of viscous heating H_S in 3D deformation (see Table 1 for symbols and units) depends on the magnitude of the deviatoric stress tensor the rock can sustain (σ) and the strain rate tensor ($\dot{\varepsilon}$), which is expressed in the equation:

$$H_S = \sigma_{xx}\dot{\varepsilon}_{xx} + \sigma_{yy}\dot{\varepsilon}_{yy} + \sigma_{zz}\dot{\varepsilon}_{zz} + 2\left(\sigma_{xy}\dot{\varepsilon}_{xy} + \sigma_{xz}\dot{\varepsilon}_{xz} + \sigma_{yz}\dot{\varepsilon}_{yz}\right) \tag{1a}$$

where $\dot{\varepsilon}_{ij} = 1/2[(\partial v_i/\partial j) + (\partial v_j/\partial i)]$, and i and j are coordinates (x, y, z). Simplifying the mode of deformation permits a reduction of Eq. (1a) as follows (e.g. Turcotte & Schubert, 2002):
(i) simple shear:

$$H_S = \dot{\gamma}_{xz}\tau_{xz} \tag{1b}$$

where $\dot{\gamma}_{xz} = \partial v_x/\partial z$ is the shear strain rate and τ_{xz} is the shear stress;
(ii) homogeneous flattening/thickening in the z direction (3D pure shear):

$$H_S = \frac{3}{2}\dot{\gamma}_{zz}\sigma_{zz} \tag{1c}$$

where $\dot{\gamma}_{zz} = \partial v_z/\partial z$ is the flattening/thickening strain rate and σ_{zz} is the deviatoric stress in the flattening/thickening direction;
(iii) shortening/extension in the x direction (2D pure shear):

$$H_S = 2\dot{\gamma}_{xx}\sigma_{xx}, \tag{1d}$$

where $\dot{\gamma}_{xx} = \partial v_x/\partial x$ is the shortening/extension strain rate and σ_{xx} is the deviatoric stress in the shortening/extension direction.

This source of heat has been argued for various geodynamic processes such as mantle convection (e.g. Hansen & Yuen, 1996; Yuen *et al.*, 2000; Gerya & Yuen, 2003a), lithospheric delamination (e.g. Schott *et al.*, 2000), plateau uplift (Yuen & Schubert, 1981), subduction (e.g. Peacock, 1992) and related 'cold plumes' (Gerya & Yuen, 2003b), slab breakoff (Gerya *et al.*, 2004) continental collision (e.g. Stüwe, 1998), shear zones (e.g. Brun & Cobbold, 1980; Leloup *et al.*, 1999) and even for microstructural processes (Tenczer *et al.*, 2001) and reaction texture formation (Stüwe & Sandiford, 1994). Nevertheless, viscous heating as a significant source of energy within the lithosphere remains rather unpopular among geologists. Below, we consider and refute the most frequent arguments used to question the concept:

First, the geological evidence for viscous heating is no more than fragmentary. But absence of evidence is not evidence of absence, and regarding viscous heating as a speculative source of energy on this basis contradicts a fundamental, intrinsic and non-removable part of thermodynamics, which is present in the law of conservation of energy (e.g. Landau & Lifshitz, 1963). Viscous heating is a mechanically ubiquitous, quantitatively well-established phenomenon that does not require geological verification.

Second, heat conduction of rocks is fast and thus allows the dissipation of the heat before it can contribute to the thermal budget of the deforming zone (e.g. Poirier *et al.*, 1979). However, heat generated within any source region is spread by conduction with a characteristic timescale (t_d) that depends on the width L of the region (e.g. Stüwe, 2002, symbols in Table 1)

$$t_d = \frac{L^2}{\kappa} \tag{2}$$

with $\kappa = k/\rho C_p$.

Thus the duration of heat dissipation via conduction grows as the square of the width (L) of the deforming/heat-producing zone (Fig. 1). For instance, if the viscous heat produced within a 100-m wide shear zone dissipates in *c.* 1000 yr, then heat generated within a 1 km wide shear zone requires *c.* 10^5 yr for a similar degree of conductive cooling. Therefore, the viscous heat produced within regionally significant zones of deformation (up to several km in thickness) will not

Table 1. Abbreviations and units.

Symbol	Meaning	Units
A_D	Material constant	$MPa^{-n}\ s^{-1}$
C_p	Isobaric heat capacity	$J\ kg^{-1}\ K^{-1}$
E	Activation energy	$kJ\ mol^{-1}$
g	Gravitational acceleration (9.81)	$m\ s^{-2}$
H_a, H_r, H_S	Heat production (adiabatic, radioactive, viscous)	$W\ m^{-3}$
k	Thermal conductivity	$W\ m^{-1}\ K^{-1}$
M	Volume fraction of melt	Dimensionless
n	Stress exponent	Dimensionless
P	Dynamic pressure	Pa
P_{fluid}	Pore fluid pressure	Pa
P_{lith}	Lithostatic pressure	Pa
q_x, q_z	Horizontal and vertical heat fluxes	$W\ m^{-2}$
Q_L	Latent heat of melting	$kJ\ kg^{-1}$
T	Temperature	K
$T_{liquidus}$, $T_{solidus}$	Liquidus and solidus temperature of the crust	K
V	Activation volume	$J\ MPa^{-1}\ mol^{-1}$
v_x,v_y,v_z	Horizontal, lateral and vertical components of velocity vector	$m\ s^{-1}$
x, y, z	Horizontal, lateral and vertical coordinates	m
α	Thermal expansion coefficient	K^{-1}
β	Compressibility coefficient	Pa^{-1}
$\dot{\varepsilon}_{ij}$	Components of the strain rate tensor	s^{-1}
$\dot{\varepsilon}_{II}$	Second invariant of the strain rate tensor	s^{-2}
γ	Time-integrated (bulk) strain	Dimensionless
$\dot{\gamma}$	Strain rate	s^{-1}
η	Viscosity	Pa s
κ	Thermal diffusivity	$m^2\ s^{-1}$
λ	Pore fluid pressure coefficient: $\lambda = P_{fluid}/P$	Dimensionless
λ_{10}	Characteristic pore fluid pressure coefficient at 10 km depth	Dimensionless
ρ	Density	$kg\ m^{-3}$
σ_{ij}	Components of the viscous deviatoric stress tensor	Pa
σ_{yield}	Yield stress	Pa
τ	Shear stress	Pa

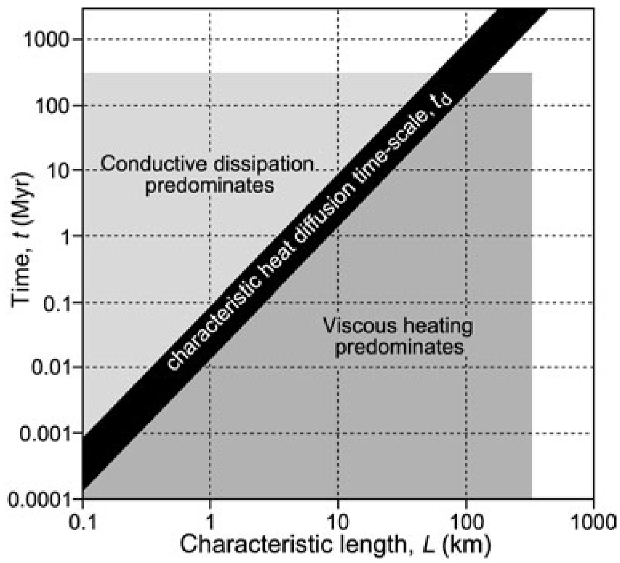

Fig. 1. Timescales for different thermal regimes calculated according to Eq. (3) with $\kappa = 10^{-6}$ m^2 s^{-1}. Shaded areas show lengths and timescales characteristic of collisional orogens.

dissipate over geologically relevant time of millions of years (Fig. 1).

Third, viscous heating is a self-destructive mechanism. As viscosity η links strain rate $\dot{\gamma}$ to shear stress τ:

$$\tau = \eta\dot{\gamma}, \tag{3}$$

(e.g. Ranalli, 1995) the responsible shear stress diminishes while generating heat and thermal softening tends to impede the system (Graham & England, 1976). In other words, as viscosity decreases as temperature increases, viscous heating decreases under constant strain rate $\dot{\gamma}$, but increases under constant shear stress. A mathematical formulation is required to define rates and temperature changes for which viscous dissipation may choke itself. If shear strain rate $\dot{\gamma}$ is kept constant, replacing shear stress τ in Eq. (1b) by its expression in Eq. (3) demonstrates that viscous heating decreases according to:

$$\frac{\partial H_S}{\partial t} = \dot{\gamma}^2 \frac{\partial \eta}{\partial t}, \tag{4}$$

provided $(\partial\eta/\partial t) < 0$.

With heat diffusion $\partial\eta/\partial t \to 0$, hence $H_S \to$ constant, which means that viscous heating becomes stable, producing a positive thermal anomaly within the deforming zone. Moreover, such H_S is non-null and so shear heating is not suppressed (e.g. Stüwe, 1998; Turcotte & Schubert, 2002). Conversely, if shear stress τ is maintained constant, then the shear strain rate $\dot{\gamma}$ increases with decreasing viscosity and, as $(\partial\eta/\partial t) < 0$, H_S actually increases with time, according to:

$$\frac{\partial H_S}{\partial t} = -\dot{\gamma}^2 \frac{\partial \eta}{\partial t} \tag{5}$$

Fourth, viscous heating is a local perturbation around shear zones and faults that require fast movement and high shear stress over long periods (Scholz, 1980), but is negligible on a regional scale. Also, assuming weakness of deeply buried rocks (e.g. Ranalli, 1995) the magnitude of temperature increase because of viscous heating is small compared with other temperature perturbations. Separating mechanical from thermal effects is a weakness of most models. The conversion of mechanical work into heat, which is a direct feedback of deformation on metamorphism, is usually neglected for the sake of simplicity but can be a significant inaccuracy. Critically, sequential or neighbouring shear-heating events are cumulative and the conductive dissipation of the heat generated does not equate to disappearance: the quantity of heat becomes distributed into a widening zone. Deformation lasting million(s) of years consists of many smaller events in time and space, ranging from grain- to kilometre-scale, distributed flow. The heat effect is additive, the dissipation time depending on the overall width of the deformation zone. This cumulative effect provides the thermal contribution because of viscous heating. As a first approximation, this thermal contribution may be estimated by integrating Eq. (1) over time t:

$$\Delta T_{\max} = \int_t \frac{H_S(t)}{\rho C_p} dt \tag{6a}$$

where $\Delta T_{\max}$ is the maximum temperature increase (assuming no heat diffusion). Under relatively constant effective regional stresses (τ_{xz},σ_{zz} or σ_{xx}), the effect of cumulative viscous heating for the different deformation modes may be estimated by integrating Eqs (1b), 1(c) and (1d) with respect to time:

(i) regional simple shear:

$$\Delta T_{\max} = \frac{\tau_{xz}\gamma_{xz}}{\rho C_p}, \tag{6b}$$

where $\gamma_{xz} = \int_t \dot{\gamma}_{xz}(t)dt$ is the bulk shear strain;

(ii) regional flattening/thickening:

$$\Delta T_{\max} = \left(\frac{3}{2}\right) \frac{\sigma_{zz}}{\rho C_p} \left| \ln\left(\frac{h_1}{h_0}\right) \right| \tag{6c}$$

where h_0 and h_1 are initial and final thicknesses, respectively;

(iii) regional shortening/extension:

$$\Delta T_{\max} = 2\frac{\sigma_{xx}}{\rho C_p} \left| \ln\left(\frac{l_1}{l_0}\right) \right|, \tag{6d}$$

where l_0 and l_1 are initial and final lengths, respectively.

The magnitudes of effective regional stresses (τ_{xz},σ_{zz},σ_{xx}) in Eqs (6b)–(6d) can be estimated from the force required to maintain the average topographic elevation h (Turcotte & Schubert, 2002, p. 223) as:

$$(\tau_{xz}, \sigma_{zz}, \sigma_{xx}) = \rho g h. \tag{7}$$

Taking $\rho = 3000$ kg m^{-3} and typical variations in topography (0.5–5 km) yields orogenic stresses of 15–150 MPa. These are minimum values as stress amplification because of deformation localization may occur in heterogeneous tectonic settings (Molnar & Lyon-Caen, 1988; Kusznir, 1991):

$$(\tau_{xz}, \sigma_{zz}, \sigma_{xx}) = \rho g h \frac{L_t}{L_d} \tag{8}$$

where L_t is the length of the deformation system and L_d is the length of the localised, actively deforming zone. These rough stress estimates are consistent with *in situ* measurements yielding values of the order of tens of MPa (e.g. Turcotte & Schubert, 2002). In the case of regional simple shear, plotting the dependence of ΔT_{max} on effective shear stress (τ_{xz}) and bulk shear strain (γ_{xz}) shows that, for conservative values of effective orogenic stress and bulk shear strain (≥1), the maximum increase in temperature reaches several tens or even hundreds of degrees (Fig. 2). Obviously, under relatively slow deformation, the actual values of temperature increase may be considerably smaller, because of heat diffusion (Fig. 1). It is worth noting that viscous heating has a strain-rate dependent timescale adjusted to progressing deformation [Eq. (1)], thus providing immediate feedback to metamorphic temperatures (Stüwe, 1998). In contrast, radiogenic heating has a timescale >1 Myr for $\Delta T_{max} = 100$ °C, independent of deformation; as discussed by Kincaid & Silver (1996), heat production because of radiogenic decay lasts five to 10 times longer than regional metamorphism dated in orogenic zones.

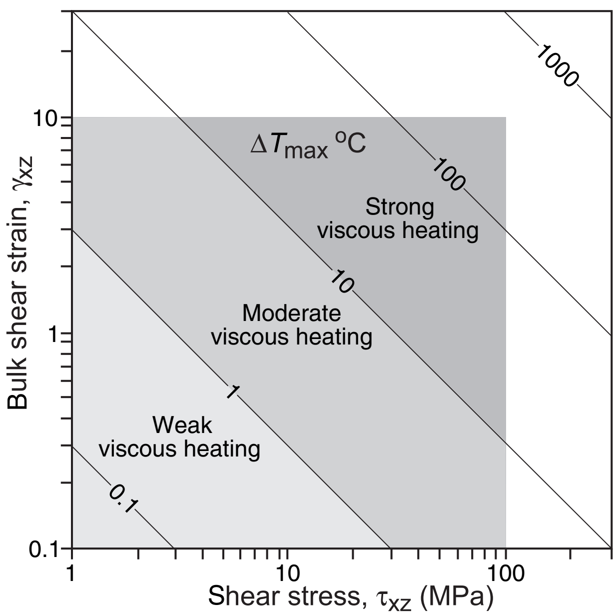

Fig. 2. Effect of viscous heating on metamorphic temperature calculated according to Eq. (6b) with $\rho = 3000$ kg m^{-3} and $C_p = 1000$ J kg^{-1} K^{-1}. Shaded areas cover strains and stresses characteristic of orogenic processes (e.g. Turcotte & Schubert, 2002).

A final argument is that fluids infiltrating along fault zones should rapidly carry heat away.

Because fluid and rock have comparable heat capacities, the mass of circulating fluids passed through rocks must be comparable to the mass of the rocks themselves to have efficient cooling effects (e.g. Connolly & Thompson, 1989). The heat balance is hardly achievable at peak metamorphic conditions. Dehydration of rocks takes place during diagenesis and the early stages of metamorphism. Higher grade rocks do not contain volume fractions of fluids large enough to remove heat produced by mechanical work.

Such qualitative considerations point towards a significant bulk effect of viscous heating during orogeny. Yet, these considerations need to be supported by quantitative estimates on both amount and dynamics of viscous heating in realistic orogenic situations. We therefore performed systematic, high resolution 2D numerical modelling of continental collision to determine both an average intensity, and the spatial and temporal patterns of viscous heat production within the deforming continental lithosphere. In order to do this in a more realistic way, numerical models of collision were developed that incorporate viscoplastic pressure–temperature–strain-rate-dependent rheology, pressure–temperature-dependent conductivity and partial melting of the crust. Details on boundary conditions and technical description of the analytical and modelling techniques are given in the Appendix. The results are applied to examine the effects of viscous heating on the thermal evolution of the central Alps.

RESULTS FROM NUMERICAL EXPERIMENTS

Thirty-seven numerical experiments using 17 configurations (Table 3) have been run with a finite-difference grid of 354×88 irregularly spaced Eulerian points (Fig. 3a), and with over 7 million markers to portray fine details of the temperature, material and viscosity fields. By varying the experimental parameters the primary interest is in quantifying the extent and the pattern of viscous heating as a function of upper- and lower-crustal compositions and rheology, and convergence rate. Our discussion essentially refers to successive stages of Model 10 (Figs 4–6) characterized by the rather slow convergence rate of 2 cm yr^{-1} and the moderate ductile strength of the crust composed of upper felsic and lower mafic layers (Tables 2 & 3). Similar evolutions were identified in other models, with variances that are discussed below.

First-order features

A double-verging geometry, which branches at the point where the mantle is subducting, occurs from the beginning (Fig. 4a,b). The strain rate distribution (Fig. 5e,f) and the Y-shaped pattern of viscous heating (Fig. 4e,f) also fit this pattern. The amount of heat

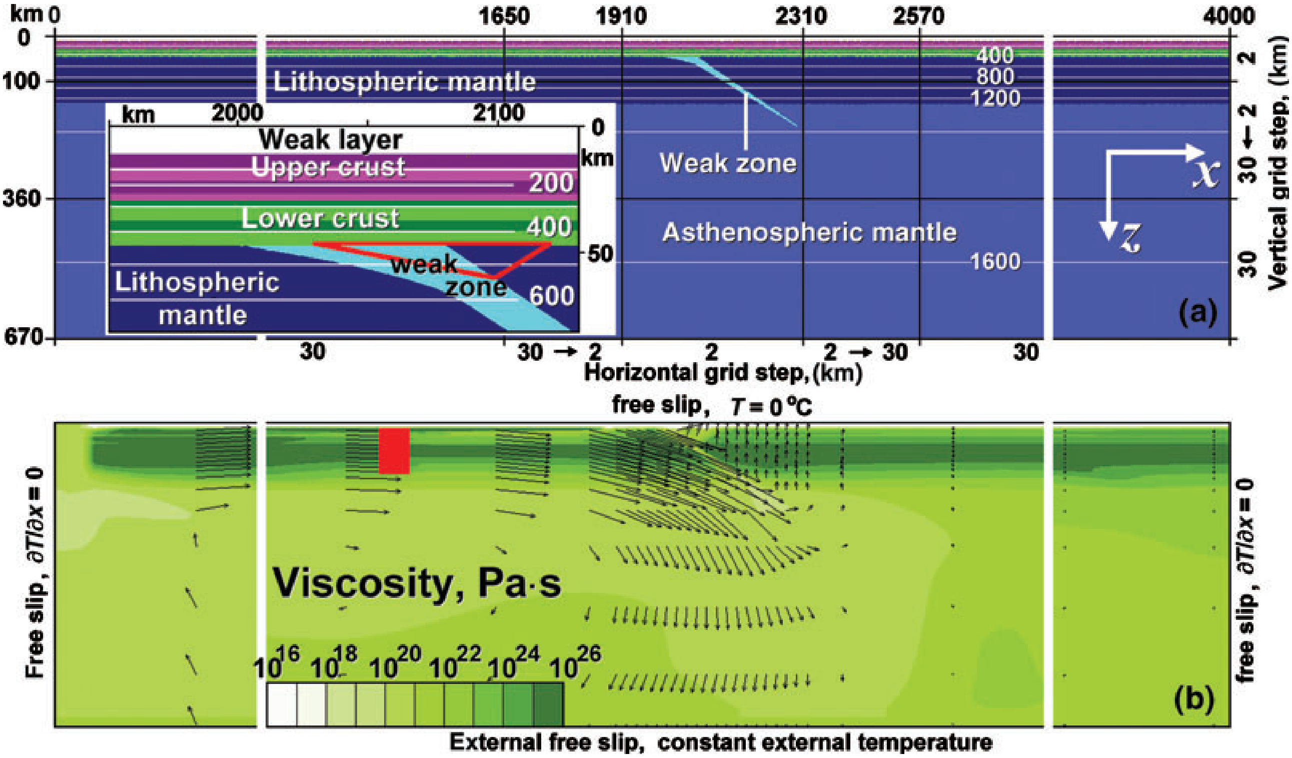

Fig. 3. Two-dimensional numerical setting employed in this study: (a) initial layering of different rock lithologies, temperature (isotherms in °C) and numerical grid steps. The lithospheric and asthenospheric mantles have the same physical properties, different colours are used for better visualization of slab deformation and structural development. This is also true for the medium scale layering within the upper and the lower crust; inset shows the initial geometry of the collision zone. Red triangle shows the wedge of lower crustal rocks imposed for some of the numerical experiments (Model 17 in Table 3). (b) initial calculated dynamic viscosity structure and boundary conditions; arrows show calculated initial flow pattern corresponding to plate convergence initiation; the red rectangle shows the *convergence condition region*.

produced by viscous dissipation is on average 0.1–0.3 μW m^{-3} (Table 3), which corresponds to 10–30% of radiogenic heat generation ($\simeq$1 μW m^{-3}) in the crust. The degree of viscous heating shows strong lateral variations and often reaches values 1–10 μW m^{-3} along localized (yet several kilometres thick) deformation zones (Fig. 4e–h). Thus, viscous heating provides an important source of heat in movement zones. The timescale for heat diffusion (t_d) within these zones is on the order of several million years (Fig. 1) and is comparable with the timescale of deformation (see timing in Fig. 4a–d), which results in noticeable positive temperature anomalies along these zones (see isotherms in Fig. 4a–d). For example, temperature along the plate interface is sufficiently increased to produce partial melting of subducted crustal rocks (Fig. 4c,d, red coloured zone).

Tectonic stress and overpressure

Figure 6 shows the distribution of deviatoric stresses and non-lithostatic pressure component in the same Model 10. Inclinations of the principal stress axes (Fig. 6a,b) fan according to the double-verging pattern. Deviatoric stresses (Fig. 6a–d) vary from 10 to 100 MPa in the crust, in accordance with estimates presented in the introduction. Strong positive (up to 100%) and negative (up to 50%) non-lithostatic pressure regions develop in the upper (brittle) part of the mantle lithosphere (Fig. 6e–h). There are no strong (> 20%) overpressures in the thickened orogenic crust; this appears to be because of the relatively low brittle strength of crustal rocks used in our numerical experiments (Table 3). However, relatively high (10–20%) overpressures (Fig. 6g,h) occur in crustal rocks at the lower tip of the wedge-shaped tectonic/subduction channel (Fig. 4d), which is equivalent to overpressures of 200–600 MPa at 70–90 km depth. These overpressures are related to the onset of the forced upward-directed return flow (Fig. 5c,d) of subducted crustal and hydrated mantle rocks from the channel contributing to the exhumation of high-pressure complexes (e.g. Dobretsov & Kirdyashkin, 1992; Mancktelow, 1995; Gerya & Stöckhert, 2002).

Effect of rheology on viscous heating

We compared the distribution of viscous heating in models with rheologically different lower crusts and different convergence rates (Fig. 7). An increase in the

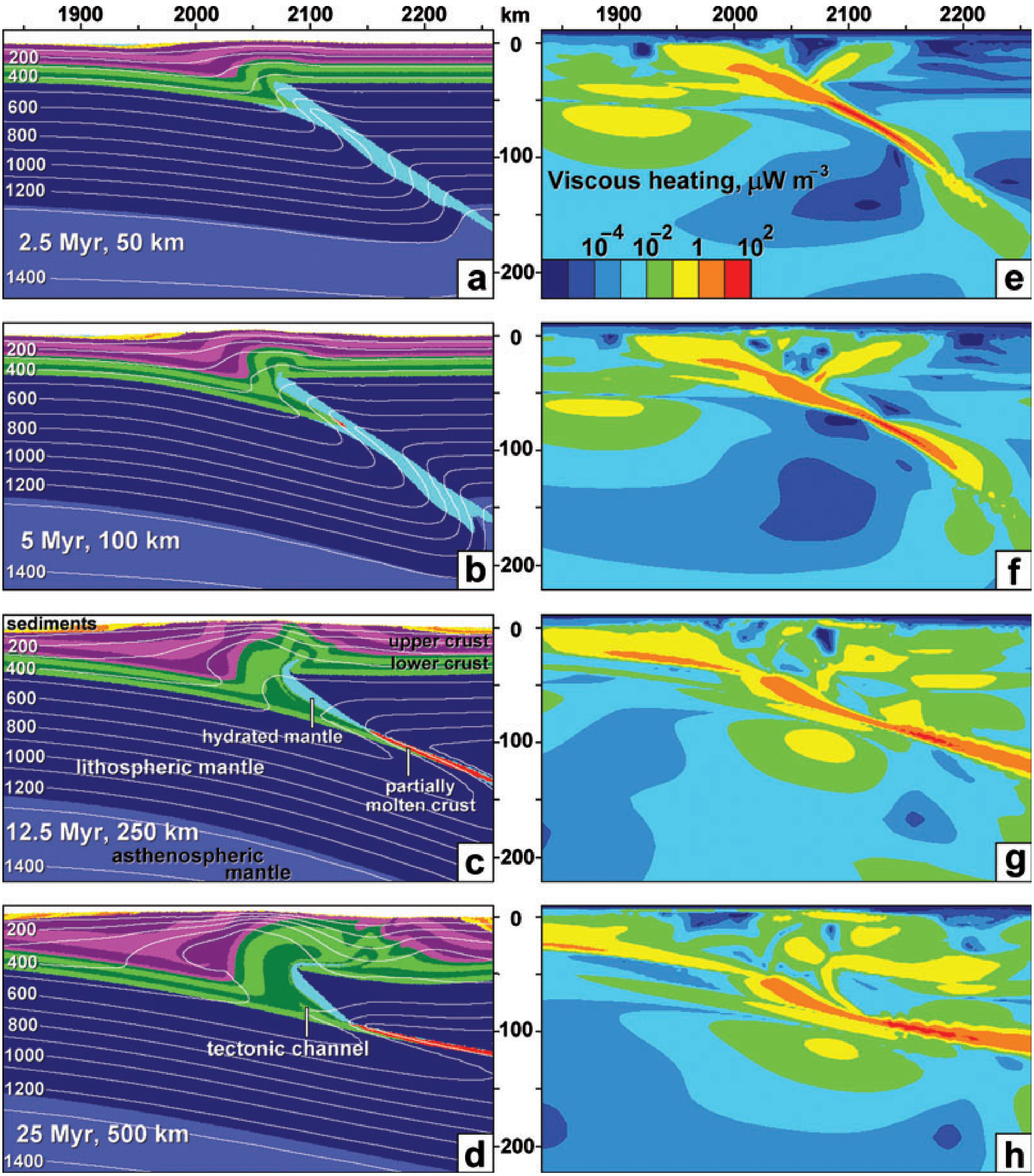

Fig. 4. Enlarged 425 × 235 km areas of the original 4000 × 670 km reference Model 10, with convergence rate = 2 cm yr^{-1} (Table 3). Left: Distribution of rock layers (as in Fig. 3a) in the collision zone during subduction of the mantle lithosphere. Time and amount of shortening are given in the figures (Myr and km, respectively). White numbered lines are isotherms in °C. Right: Viscous heating at corresponding collision steps in left column. Vertical scale: depth below the z = 10 km sea level.

convergence rate causes a proportional increase in the amount of viscous heating in the crust for the same amount of shortening (compare Model 10 to Model 14, and Model 15 to Model 16; Table 3). Models with relatively strong lower crusts (dominated by plagioclase creep) develop significant amounts of viscous heating in the crust (0.18–0.46 μW m^{-3} after 150 km of convergence, Table 3) and produce structural domes

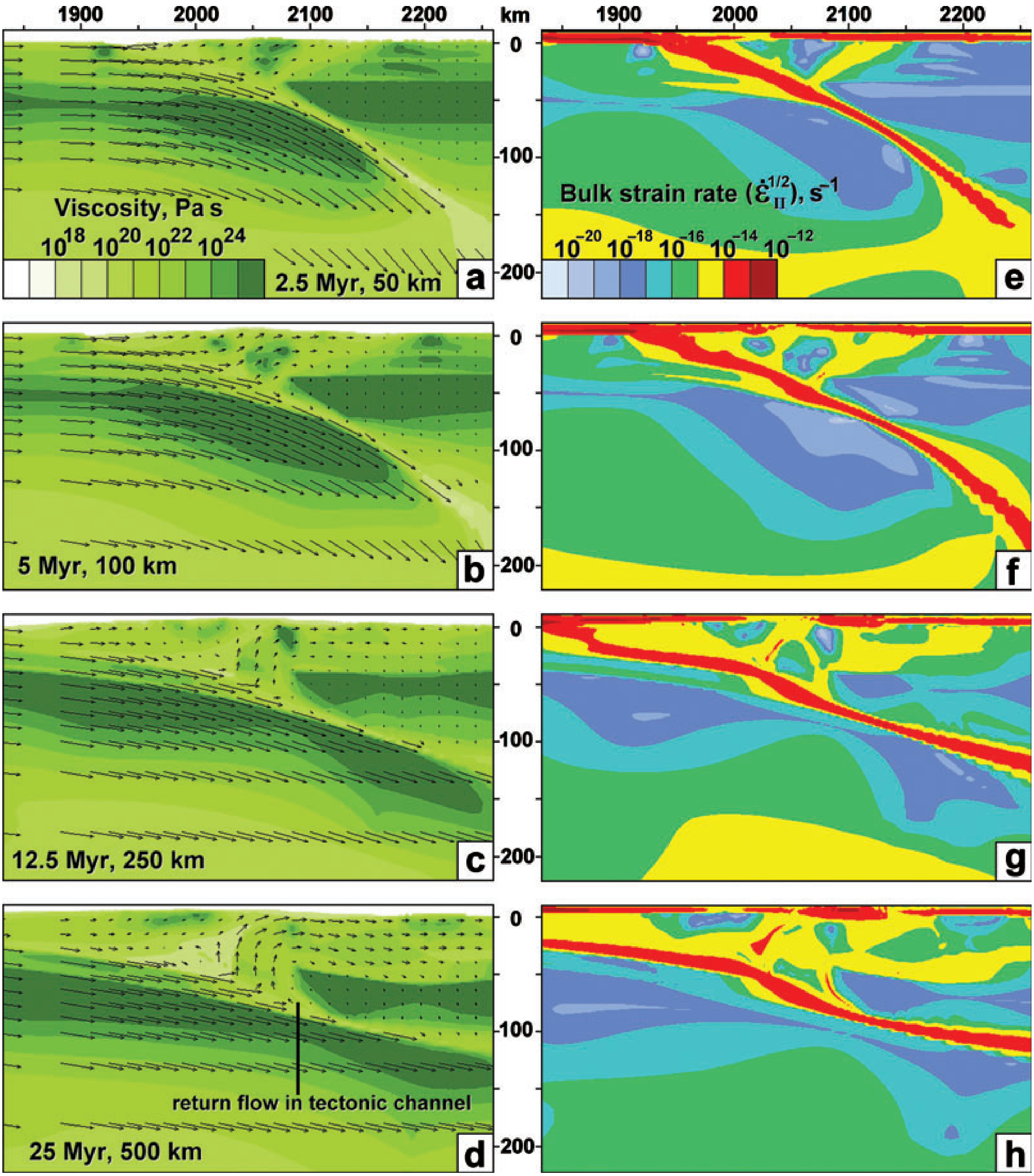

Fig. 5. Enlarged 425 × 235 km area of the original 4000 × 670 km reference Model 10, with convergence rate = 2 cm yr^{-1} (Fig. 4; Table 3). Left: Viscosity fields for corresponding shortening (km)/time (Myr) stages; arrows show the calculated velocity field. Right: Strain rate (square root of second invariant of strain rate tensor $\dot{\varepsilon}_{II} = 1/2\dot{\varepsilon}_{ij}\dot{\varepsilon}_{ij}$ shown as colour code). Vertical scale as in Fig. 4.

of 10–15 km amplitude that facilitate exhumation of lower crustal rocks. Models with weak lower crusts (dominated by wet quartzite creep) show insignificant viscous heating in the crust (0.02–0.06 $\mu W\ m^{-3}$ after 150 km of convergence, Table 3), while fundamentally homogeneous crustal thickening does not allow exhumation of deeper crustal rocks. Therefore, the general cross-sectional structure of the orogen (Fig. 7a–d)

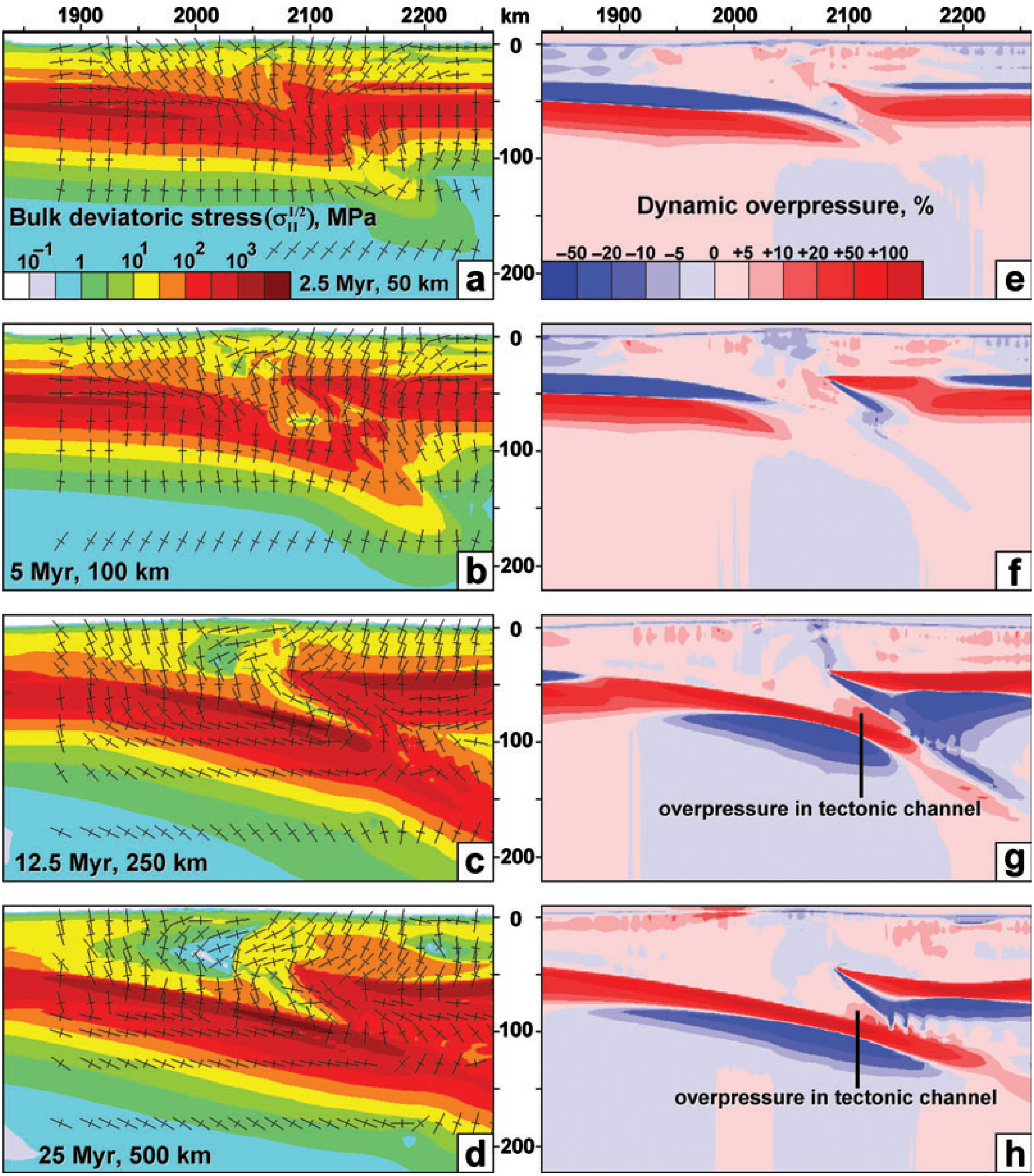

Fig. 6. Enlarged 425 × 235 km area of the original 4000 × 670 km reference Model 10, with convergence rate = 2 cm yr^{-1} (Fig. 4; Table 3). Left: Stress fields (square root of second invariant of deviatoric stress tensor $\sigma_{II} = 1/2\sigma_{ij}\sigma_{ij}$ shown as colour code) for corresponding shortening (km)/time (Myr) stages; long and short branches of elongated crosses show orientations of largest and smallest principal stress axes, respectively. Right: Distributions of the non-lithostatic pressure component $\Delta P = 100(P - P_{lith})/P_{lith}$. Vertical scale as in Fig. 4.

as well as the intensity of *crustal* viscous heating (Fig. 7e–h) strongly reflects the rheological strength of the lower crust. On the other hand, all models show strong viscous heating in the mantle (Fig. 7e–h, Table 3) along the upper surface of the subducting slab, where temperatures trigger partial melting of mantle rocks.

Table 2. Material properties[a] used in 2D numerical experiments.

Material	ρ_0 (kg m^{-3})	k (W m K^{-1})	$T_{solidus}$ (K)	$T_{liquidus}$ (K)	Q_L (kJ kg^{-1})	H_r(μW m^{-3})	Flow law	E (kJ mol^{-1})	n	A_D (MPa^{-n} s^{-1})	V (J MPa^{-1} mol^{-1})
Felsic and sedimentary crust	2800 (solid) 2400 (molten)	$[0.64 + 807/(T + 77)] \times \exp(0.00004\ P_{MPa})$	$889 + 17\,900/(P + 54) + 20\,200/(P + 54)^2$ at $P < 1200$ MPa $831 + 0.06\ P$ at $P > 1200$ MPa	$1262 + 0.09\ P$	300	1–1.75	Wet quartzite	154	2.3	$10^{-3.5}$	0
Mafic crust	3000 (solid) 2900 (molten)	$[1.18 + 474/(T_K + 77] \times \exp(0.00004\ P_{MPa})$	$973–70\,400/(P + 354) + 77\,800\,000/(P + 354)^2$ at $P < 1600$ MPa $935 + 0.0035\ P + 0.0000062\ P^2$ at $P > 1600$ MPa	$1423 + 0.105\ P$	380	0.25	Plagioclase An_{75}	238	3.2	$10^{-3.5}$	0
Lithosphere–asthenosphere dry mantle	3300	$[0.73 + 1293/(T_K + 77] \times \exp(0.00004\ P_{MPa})$	–	–	–	0.022	Dry olivine	532	3.5	$10^{4.4}$	8
Hydrated mantle in subduction shear zone	3300	$[0.73 + 1293/(T_K + 77] \times \exp(0.00004\ P_{MPa})$	–	–	–	0.022	Wet olivine	470	4	$10^{3.3}$	8
References[b]	1, 2	3	4	4	1, 2	1	5	5	5	5	1, 5

[a] $C_p = 1000$ J kg^{-1} K^{-1}, $\alpha = 3 \times 10^{-5}$ K^{-1}, $\beta = 1 \times 10^{-5}$ Mpa^{-1} for all rock types.
[b] 1, Turcotte & Schubert (2002); 2, Bittner & Schmeling (1995); 3, Clauser & Huenges (1995); 4, Schmidt & Poli (1998); 5, Ranalli (1995).

Local perturbations of metamorphic temperatures

As follows from Fig. 1, viscous heating produced in deformation zones of several kilometre thickness (Fig. 5e–h) should have important local effects on the metamorphic temperature when deformation takes place on the timescale of several million years or shorter. Positive temperature anomalies along deformation zones should therefore be characteristic of relatively fast convergence rates. This conclusion is supported by comparing two cases using the same numerical setup as for experiment 14 but with a higher convergence rate of 5 cm yr^{-1}. In one case viscous heating is ignored (Fig. 8a–d), in the other case (Fig. 8e–h), viscous heating contributes to the thermal pattern. From Fig. 8i–l, it can be readily seen that viscous heating (i) provides a significant (25–200 °C) increase in metamorphic crustal temperatures (Fig. 8i–l), (ii) facilitates upwelling of lower crustal rocks (Fig. 8d,h), (iii) triggers melting of the subducted crust at the plate interface (Fig. 8c,g), and (iv) produces decoupling and decreases bending of the plates (Fig. 8d,h).

Temporal variability and overall intensity of viscous heating

Under a constant convergence rate, the amount of viscous heating tends to decrease with time (Fig. 9a, Table 3) while viscosity decreases (Fig. 5a–d) with increasing temperature (Fig. 4a–d). The amount of viscous heating at mantle depths remains more stable (Fig. 9b, Table 3) and generally exceeds 10 μW m^{-3} along the plate interface (Figs 4e–h & 7e–h). For models with constant horizontal stresses, increase and decrease of convergence rate and viscous heating with time are both obtained (cf. Models 2, 5, 7, 9, 11; Table 3, Fig. 9). The configuration and position of the *convergence condition domain* has no significant influence on the numerical results. For example, the reference Model 10 (Table 2) with convergence velocity defined within *the mantle lithosphere only* shows shear heating intensity and dynamics very similar to those of Model 12, for which the convergence velocity was defined within *both the crust and the mantle lithosphere* (Table 3, Fig. 9).

A pronounced positive correlation is found between the overall intensity of crustal viscous heating and *instantaneous* convergence rate (Fig. 10). This correlation suggests that a significant contribution (>0.1 μW m^{-3}) of viscous heating into the crustal heat balance can be expected when the convergence rate exceeds 1 cm yr^{-1}, particularly if the lower crust is strong. Therefore, viscous heating may become a dominant heat source in collision orogens with rapid convergence rates (e.g. Himalayas).

GEOLOGICAL APPLICATION

Stüwe (1998) suggested that shear (dissipative) heat, episodically released during nappe stacking, contributed

Table 3. Parameters of selected numerical experiments.

	Upper crust			Lower crust				Convergence condition		Convergence			Topography[b] (km)		H_S^c (μW m^{-3})	
Model	Material[a]	λ_{10}	H_r (μW m^{-3})	Material[a]	λ_{10}	H_r (μW m^{-3})	$v_{s0} = v_{e0}$ (mm a^{-1})	Domain (km)	Type	Amount (km)	Rate (cm a^{-1})	Time (Myr)	Relief	Maximal altitude	At 50 km depth	At 100 km depth
1 (buad)	Strong felsic[d]	0.75	1	Strong felsic[d]	0.75	1	1	$x = 1410$–1440; $z = 55$–57	$v_x = 5$ cm a^{-1}	0	5	0	0	0	0.55	0.51
										100	5	2.0	3.7	2.9	0.43	0.45
										250	5	5.0	4.0	3.5	0.38	0.51
										500	5	10.0	6.3	5.3	0.29	0.52
2 (buaf)	Strong felsic[d]	0.75	1	Strong felsic[d]	0.75	1	1	$x = 1425$–1455; $z = 55$–57	$\sigma_{xx} = -100$ MPa	0	0.7	0	0	0	0.07	0.06
										100	1.6	8.0	2.3	1.9	0.09	0.14
										250	0.5	31.0	1.5	2.1	0.01	0.04
										450	0.8	66.2	2.1	2.3	0.03	0.04
3 (buag)	Strong felsic[d]	0.75	1	Strong felsic[d]	0.75	1	1	$x = 1410$–1440; $z = 55$–57	$v_x = 3$ cm a^{-1}	0	3	0	0	0	0.31	0.28
										100	3	3.3	3.3	2.6	0.23	0.26
										250	3	8.3	3.4	3.5	0.19	0.30
										500	3	16.6	4.4	3.7	0.17	0.32
4 (buah)	Felsic	0.75	1	Felsic	0.75	1	1	$x = 1410$–1440; $z = 55$–57	$v_x = 5$ cm a^{-1}	0	5	0	0	0	0.39	0.43
										100	5	2.0	0.9	0.8	0.09	0.30
										250	5	5.0	0.8	1.1	0.07	0.52
										500	5	10.0	1.6	1.8	0.06	0.51
5 (buai)	Felsic	0.75	1	Felsic	0.75	1	1	$x = 1425$–1455; $z = 55$–57	$\sigma_{xx} = -100$ MPa	0	0.9	0	0	0	0.05	0.05
										100	9.6	2.5	1.3	1.0	0.24	0.50
										250	6.0	5.1	0.8	1.1	0.09	0.47
										450	0.4	14.5	0.8	1.1	0.01	0.06
6 (buaj)	Felsic	0.75	1.75	Mafic	0.9	0.25	1	$x = 1410$–1440; $z = 55$–57	$v_x = 3$ cm a^{-1}	0	3	0	0	0	0.39	0.53
										100	3	3.3	8.0	3.4	0.34	0.42
										250	3	8.3	10.4	5.6	0.34	0.37
										500	3	16.6	6.3	5.4	0.22	0.27
7 (buak)	Felsic	0.75	1.75	Mafic	0.9	0.25	1	$x = 1425$–1455; $z = 55$–57	$\alpha_{xx} = -200$ MPa	0	4.9	0	0	0	0.68	0.97
										100	20.0	0.9	12.5	2.9	3.11	3.12
										193	26.2	1.4	10.8	3.3	4.94	3.92
										385	41.7	2.0	21.0	6.8	6.81	5.49
8 (bual)	Felsic	0.9	1.75	Mafic	0.9	0.25	1	$x = 1410$–1440; $z = 55$–57	$v_x = 1$ cm a^{-1}	0	1	0	0	0	0.11	0.15
										100	1	10.0	5.9	3.4	0.07	0.12
										250	1	25.0	5.0	3.9	0.05	0.12
										500	1	50.0	4.6	3.6	0.02	0.07
9 (buam)	Felsic	0.9	1.75	Mafic	0.9	0.25	0.3	$x = 1425$–1455; $z = 55$–57	$\sigma_{xx} = -100$ MPa	0	1.1	0	0	0	0.13	0.18
										50	3.7	4.7	5.0	1.7	0.38	0.63
										95	14.6	5.3	7.4	3.5	1.67	2.32
10 (buan)	Felsic	0.9	1.75	Mafic	0.9	0.25	0.6	$x = 1410$; $z = 51$–93	$v_x = 2$ cm a^{-1}	0	2	0	0	0	0.23	0.33
										100	2	5.0	6.4	4.1	0.17	0.25
										250	2	12.5	6.8	5.3	0.16	0.27
										500	2	25.0	5.8	5.4	0.10	0.27
11 (buao)	Felsic	0.9	1.75	Mafic	0.9	0.25	0.3	$x = 1425$; $z = 47$–69	$\sigma_{xx} = -300$ MPa	0	0.5	0	0	0	0.05	0.07
										24	0.06	41.9	1.9	0.9	0.005	0.006
12 (buap)	Felsic	0.9	1.75	Mafic	0.9	0.25	0.6	$x = 900$; $z = 11$–69	$v_x = 2$ cm a^{-1}	0	2	0	0	0	0.24	0.34
										100	2	5.0	6.5	4.1	0.17	0.25
										150	2	7.5	7.9	5.0	0.18	0.24
										250	2	12.5	6.7	5.3	0.16	0.27
										350	2	17.5	7.2	6.0	0.13	0.31
13 (buar)	Felsic	0.9	1.75	Mafic	0.9	0.25	3	$x = 900$; $z = 11$–69	$v_x = 5$ cm a^{-1}	0	5	0	0	0	0.63	0.96
										100	5	2.0	6.9	4.2	0.46	0.65
										250	5	5.0	8.1	6.2	0.49	0.60
										500	5	10.0	7.8	6.8	0.39	0.52

14 (buas[e])	Felsic	0.9	1.75	Mafic	0.9	0.25	3	$x = 900$; $z = 11$–69	$v_x = 5$ cm a^{-1}	0	5	0	0	0	0.57	0.86
										100	5	2.0	6.2	4.3	0.44	0.62
										150	5	3.0	7.8	5.4	0.46	0.58
										250	5	5.0	7.6	5.7	0.41	0.59
										500	5	10.0	5.4	4.4	0.20	0.39
15 (buat[e])	Felsic	0.9	1	Felsic	0.9	1	3	$x = 900$; $z = 11$–69	$v_x = 5$ cm a^{-1}	0	5	0	0	0	0.35	0.45
										105	5	2.1	0.8	0.9	0.07	0.35
										150	5	3.0	0.8	1.0	0.06	0.42
										260	5	5.2	1.0	1.3	0.05	0.44
16 (buau)	Felsic	0.9	1	Felsic	0.9	1	0.6	$x = 900$; $z = 11$–69	$v_x = 2$ cm a^{-1}	0	2	0	0	0	0.14	0.17
										95	2	4.75	0.5	0.6	0.02	0.15
										150	2	7.5	0.6	0.8	0.02	0.16
										180	2	9.0	0.7	0.9	0.02	0.18
17 (bubd[f])	Strong felsic[d]	0	1	Mafic	0	0.25	5	$x = 900$; $z = 11$–69	$v_x = 5$ cm a^{-1}	0	5	0	0	0	1.55	1.64
										165	5	3.3	14.2	7.3	1.56	1.33
										200	5	4.0	13.7	5.9	1.618	1.58

[a] See Table 2 for default parameters.
[b] Relief and maximal altitude (above the $z = 10$ km sea level calculated for 1850–2250 km interval above the collision zone.
[c] Average viscous heat production by 50 and 100 km depth (below the $z = 10$ km sea level) calculated for 1850–2250 km interval within the collision zone.
[d] Strong rheology is implemented by decreasing the A_D value in Eq. (11) by a factor of 100.
[e] $\lambda_{10} = 0.5$ is used for dry mantle (0 and 0.9 are default values of λ_{10} for respectively, dry and hydrated mantle in all numerical experiments).
[f] 15 km deep and 90 km wide wedge composed of lower crustal rocks has been initially posed in the bottom of the crust at the plate boundary (Fig. 3a).

significantly to thermal perturbations in the Eastern Alps. In the present paper we draw attention to the Lepontine Dome (Fig. 11), a prominent structural dome of the post-Mid-Eocene Central Alps delineated by the concentric distribution of isograds that cut earlier, Cretaceous to Eocene contacts of the Penninic nappe pile (Wenk, 1956; Trommsdorff, 1966; Niggli, 1970). This relationship suggests a time lag, not discussed here, between high pressure/temperature syn-nappe metamorphism, and the lower pressure/temperature Lepontine thermal event summarized in Fig. 12. Previous authors have attributed this thermal pattern to (i) subduction of crustal fragments rich in heat-generating radioactive elements (e.g. Goffé *et al.*, 2003 and references therein) or (ii) extrusion of hot crustal units previously subducted to mantle depth (Engi *et al.*, 2001). Modelling of these processes applied to the Alps had to include a highly radiogenic crust and/or viscous heating to obtain agreement with geological information (Roselle & Engi, 2002). Analogue modelling shows that crustal subduction during the formation of the Lepontine is a mechanically disputable hypothesis (Burg *et al.*, 2002) and high-resolution tomography reveals subduction of the European mantle lithosphere only (Lippitsch *et al.*, 2003). These observations persuaded us to examine the effects of viscous heating produced by Oligocene–Miocene crustal imbrication on the thermal evolution of the Central Alps during subduction of the mantle lithosphere.

Lepontine Dome

The 40 Myr-old high-pressure mineral assemblages suffered rapid decompression in the early stages of the development of the Lepontine Dome (Gebauer, 1999). The thermal overprint is dated at 38–35 Ma near the northern margin of the dome and peak metamorphic temperatures were established over most of the Lepontine at *c*. 32 Ma (see details and methods in Hunziker *et al.*, 1992; Gebauer, 1999). More generally, metamorphic conditions lasted from 35 to 25 Ma (Grujic & Mancktelow, 1996; Frey & Mählmann, 1999). Thermobarometry documents an increase in peak metamorphic temperatures from 500–550 °C at the northern limit of the dome to 680 °C at the southern border, against the Insubric Line (Fig.13, Engi *et al.*, 1995). Highest temperatures do not match maximum metamorphic pressures of *c*. 7 kbar in the core. Pressures decrease asymmetrically northward (to 5.5 kbar) and southward (down to 4.5 kbar; Engi *et al.*, 1995; Todd & Engi, 1997). In terms of thermobarometric uncertainties, these differences in *P–T* conditions might not be as large as stated. In any case, they portray, along with the age ranges, the finite state of a diachronous, Barrovian-type metamorphic field (Engi *et al.*, 1995). Rb–Sr and Ar–Ar ages of *c*. 21–23 Ma in the centre and 28 Ma in the south (Engi *et al.*, 1995) refer to already dominant cooling stages. Fission track ages

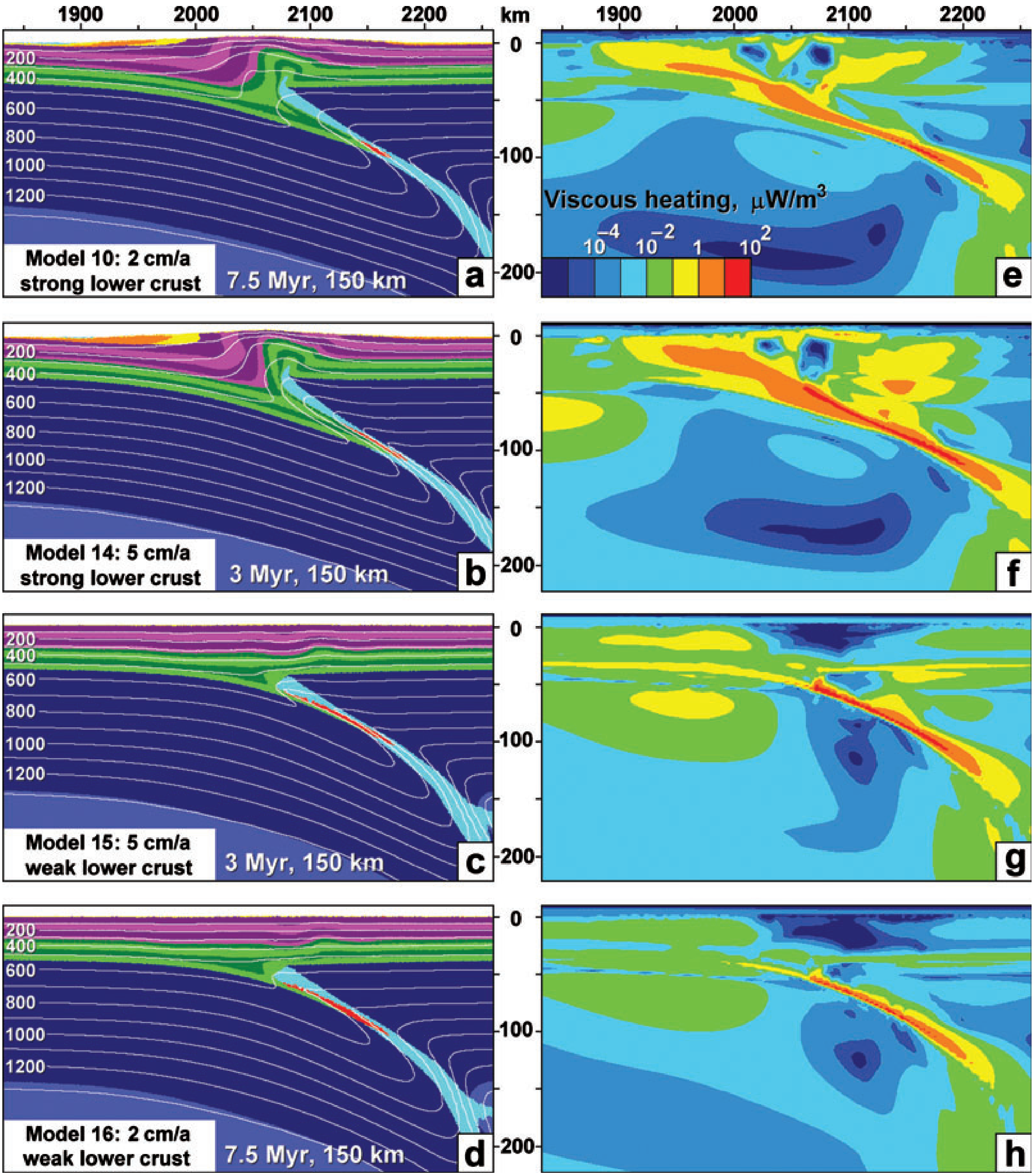

Fig. 7. Comparison of different models at 150 km convergence. Each sketch represents an enlarged 425 × 235 km area of the original 4000 × 670 km models (Table 3). Left: Distribution of different rock types (same colour code as Fig. 4); isotherms in °C. Right: Viscous heating distribution. Vertical scale as in Fig. 4.

of detrital grains suggest that the core of the Lepontine became exposed at *c.* 14 Ma (Spiegel *et al.*, 2000) and cooling/exhumation continued after then (Grasemann & Mancktelow, 1993). Zones of rapid cooling migrated from the east to the west but geological and geochronological data are insufficient to differentiate erosion-dominated versus tectonic-dominated denudation (Schlunegger & Willett, 1999).

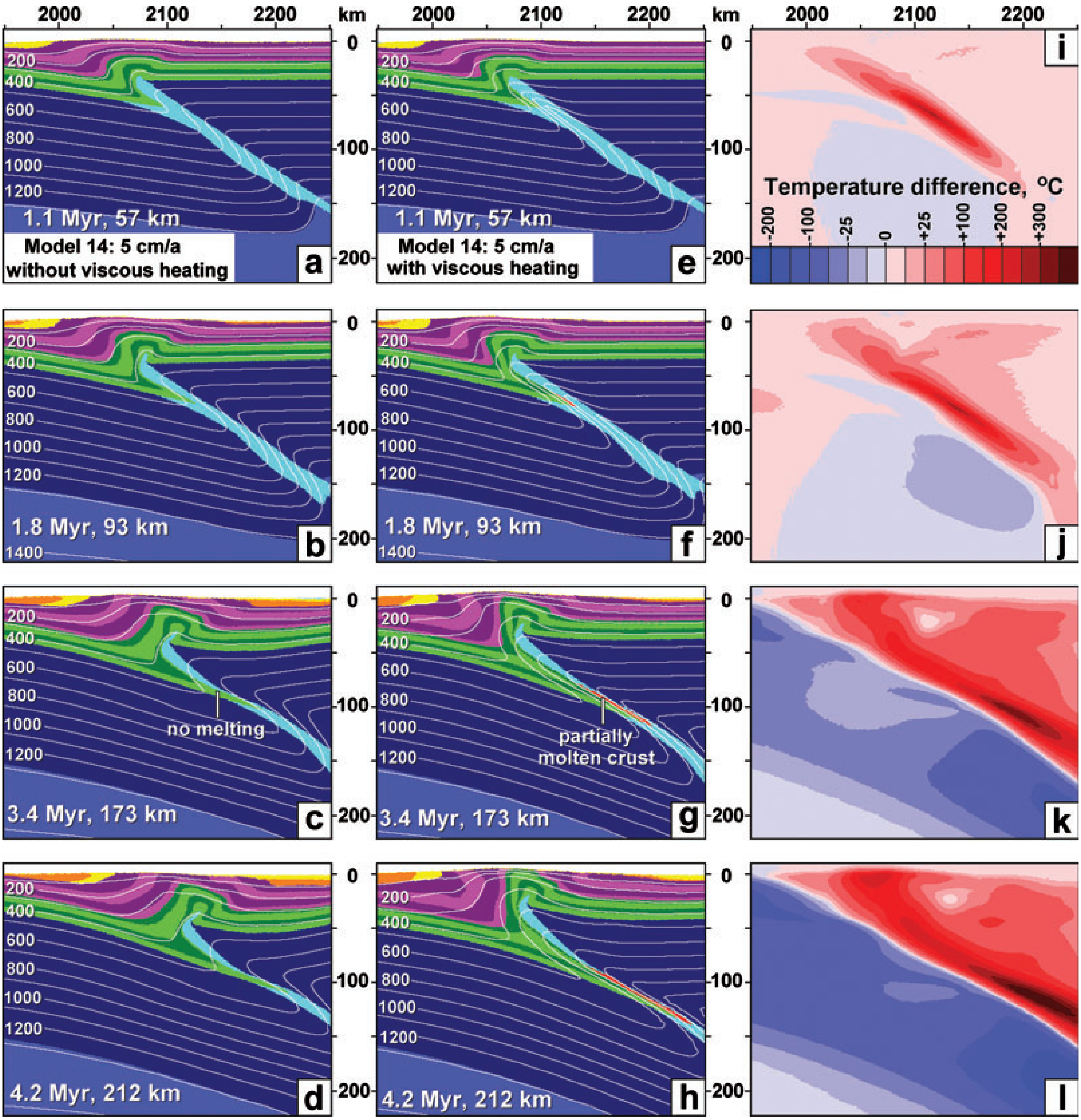

Fig. 8. Influence of viscous heating on the thermal regime and structure of the collision orogen. Each sketch represents an enlarged 300 × 235 km area of the original 4000 × 670 km Model 14 (Table 3). Vertical scale as in Fig. 4. Left column: model development with no viscous heating. Middle column: model development with viscous heating. Right column: temperature difference between equivalent stages in left and right columns. Rock types and isotherms as in Fig. 4. The negative temperature difference within the subducting mantle slab reflects the steeper subduction angle in the case of viscous heating.

In brief, the Lepontine Dome is a short-lived (< 20 Ma) thermal event accompanied by decompression during overall shortening of the area.

Strain

A wealth of structural data within the Lepontine Dome documents polyphase and penetrative deformation that has absorbed an important part of the shortening strain (Merle *et al.*, 1989; Steck & Hunziker, 1994; Grujic & Mancktelow, 1996; Rütti, 2001). Syn-metamorphic, Lepontine-related structures have isoclinally refolded often-transposed older foliations. The regional kinematics are imprecise, yet involved SW-vergent folding that intensifies towards the south where top-to SE shear is identified (Nagel *et al.*, 2002). Intense shear strain is

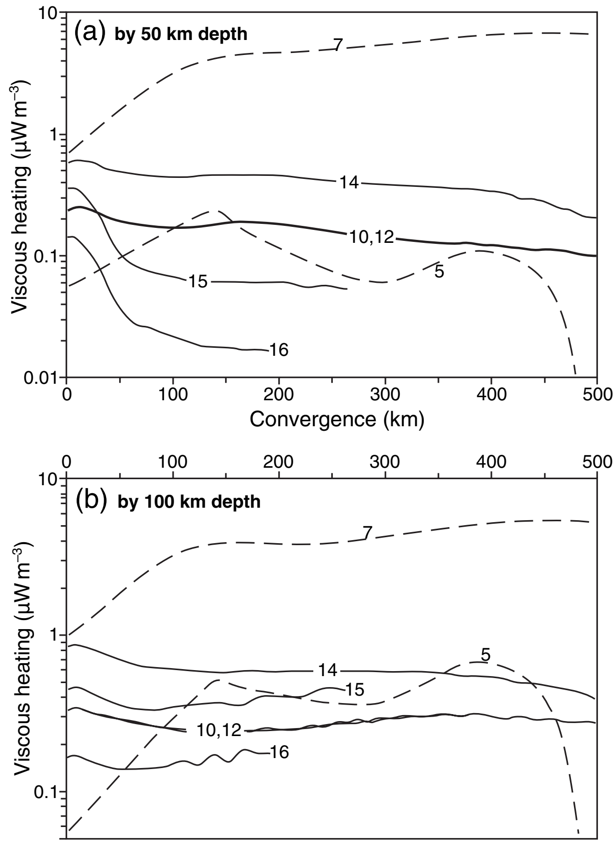

Fig. 9. Dynamics of orogenic viscous heating for selected numerical experiments (model numbers in Table 3) (a) averaged by 50 km depth (below the $z = 10$ km sea level) and (b) averaged by 100 km depth. Solid lines – models with prescribed rate of convergence (v_x). Dashed lines – models with prescribed horizontal deviatoric stress (σ_{xx}) whose rate of convergence (v_x) changes with time (Table 3).

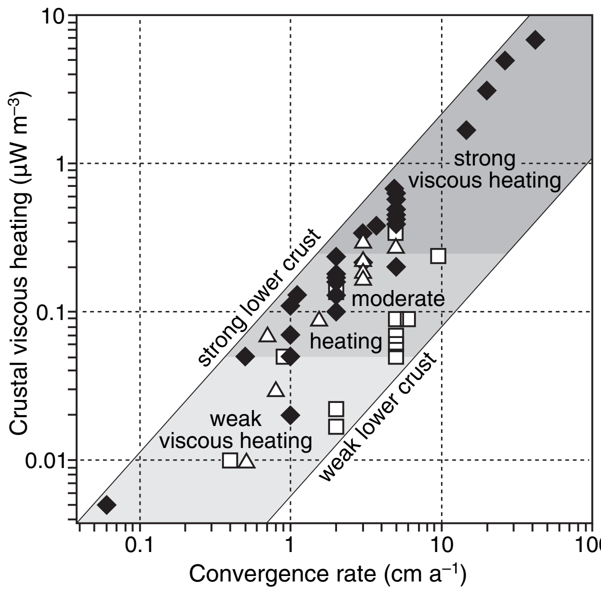

Fig. 10. Correlation between extent of viscous heating in the collision zone (1850–2250 km) expressed as an average by 50 km depth (below the $z = 10$ km sea level) with instantaneous convergence rate (Table 3). Different regimes of crustal viscous heating shown in different greyscales are arbitrarily subdivided by comparison to the average radioactive heating for the entire continental crust used in this work ($\simeq 1\ \mu$W m^{-3}, Table 2). Different symbols correspond to different rheologies of the ductile lower crust (Table 3): open squares, wet quartzite; open triangles, strong wet quartzite; solid diamonds, plagioclase.

indicated by the ubiquitous, dominant foliation bearing a marked stretching and mineral lineation parallel to fold axes, along with isoclinal folds with inverted limbs several hundreds of metres in length (e.g. Grujic & Mancktelow, 1996; Rütti, 2001). This is consistent with the concept that shear is the likely dominant orogenic deformation process (Burg, 1999), because of the tendency of the lithosphere to undergo shear failure rather than bulk flattening.

Structural information can only yield a minimum estimate of the shear strain, which can be obtained in two ways: (1) using the large-scale, tectonic information and (2) using the internal bulk fabric of the deformed zone. In this first-order approach, we ignore strain related to transcurrent deformation between Europe and Apulia (e.g. Laubscher, 1988) is ignored, which would add to the estimates presented here.

Large-scale information

The amount of convergence across the Central Alps since 40 Ma is 150 ± 50 km, most of which took place within the Lepontine Dome and the adjacent Southern Alps (Schmid *et al.*, 1996; Escher & Beaumont, 1997). Owing to large uncertainties, it is assumed (as a first approximation) that all of the convergence is accommodated by the Lepontine Dome and that omission of the few 10s kilometres shortening in the Southern Alps part of the section approximately balances, within the uncertainties given above, missing strain information in the gneiss region. The present day width of the Lepontine Gneiss Dome is *c.* 50 km, from the amphibolite facies isograd to the Insubric Line (Fig. 11). Shortening (shortening strain = $(l-l_0)/l_0$, with l and l_0 the final and initial profile lengths, respectively, e.g. Ramsay, 1967) is thus 50–75%. In the absence of quantitative information, and recognizing the uncertainty in the structural information, half of this shortening is attributed to distributed strain within the rocks. Taking into account the intense, synmetamorphic fabric described by all authors in the region, it is a very crude but fair estimate that is consistent with the 20–30% shortening commonly associated with the presence of strong foliation planes (Ramsay & Huber, 1983). It is assumed that relative movements along shear zones have taken up the remaining half. Conservative estimates thus yield distributed strain ranging from 20 to 35%. This amount of shortening was mostly achieved within 15–30 Myr, depending on the bounding age criteria chosen. These approximations

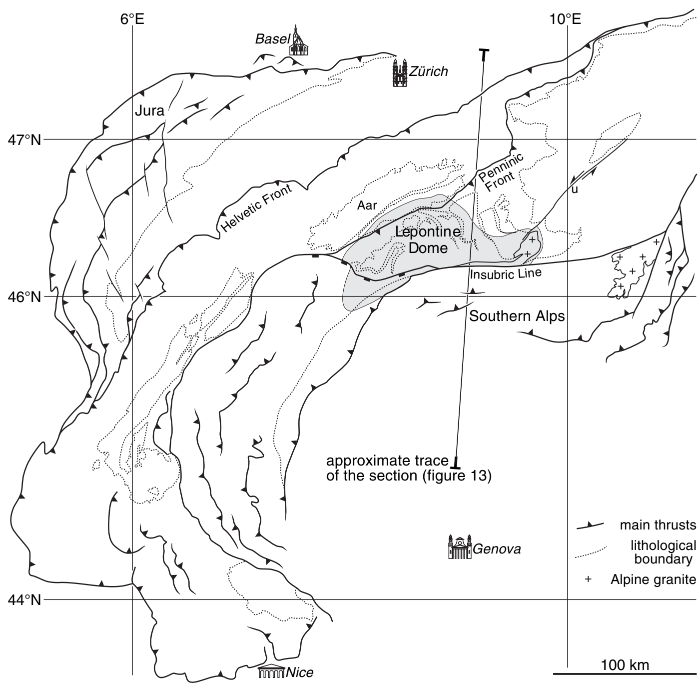

Fig. 11. Location of the Lepontine Dome in a structural sketch of the post Eocene Alps (main tectonic features only). The amphibolite facies isograd bounds the thermal dome (Steck & Hunziker, 1994).

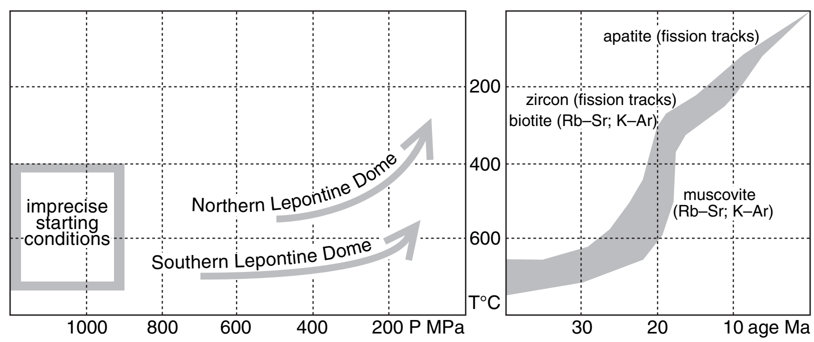

Fig. 12. Summary of the metamorphic information on the Lepontine Dome. Pressure–temperature data redrawn mostly after Engi *et al.* (1995). Cooling history with associated thermochronology redrawn after Schlunegger (1999).

imply a time-averaged convergence rate spanning 1.0–3.5 cm yr^{-1}, which is consistent with plate tectonic reconstitutions for the Alps (e.g. Schmid *et al.*, 1996).

Fabric information

The fabric developed synchronous with Lepontine metamorphism has almost completely obliterated and transposed older structures in this region. Visual transposition is reached once superimposed planes make an angle smaller than 5°, and hence is difficult to decipher and measure. The oldest foliation is often reworked by shear zones of the main syn-metamorphic deformation, thus is close to the shear plane of non-coaxial deformation identified from sense-of-shear criteria. Assuming that the dominant foliation results from simple shear, the angular relationship θ between shear and foliation planes indicates shear strain $\gamma = 2/\tan 2\theta$ (Ramsay & Graham, 1970). An angle of 5° corresponds to $\gamma \approx 11$. However, deformation is not simple shear because there are pure shear and/or volume loss components (Marquer *et al.*, 1996). Under general shear, θ used for a shear strain calculation is incorrect and the measured angle between shear and foliation planes may be only half the θ value (Burg & Laurent, 1978; Platt & Behrmann, 1986). Introducing this logic, a conservative regional shear strain of $\gamma_{xz} \geq 5$ results. Structural geologists have established that most mylonitic shear zones formed at $\gamma_{xz} \gg 10$ (e.g. Simpson, 1983; Watts & Williams, 1983; Burks & Mosher, 1996; Dutruge & Burg, 1997). The mylonitic character of the main deformation phase throughout the Lepontine Dome suggests that a regional figure of $\gamma_{xz} \geq 5$ is a plausible minimum.

Viscous heating in the Lepontine Dome

According to Eq. (6b) the upper limit of temperature increase because of a shear strain of 5 distributed over the Lepontine Dome would be $\Delta T_{\max} = 25$–250 °C for

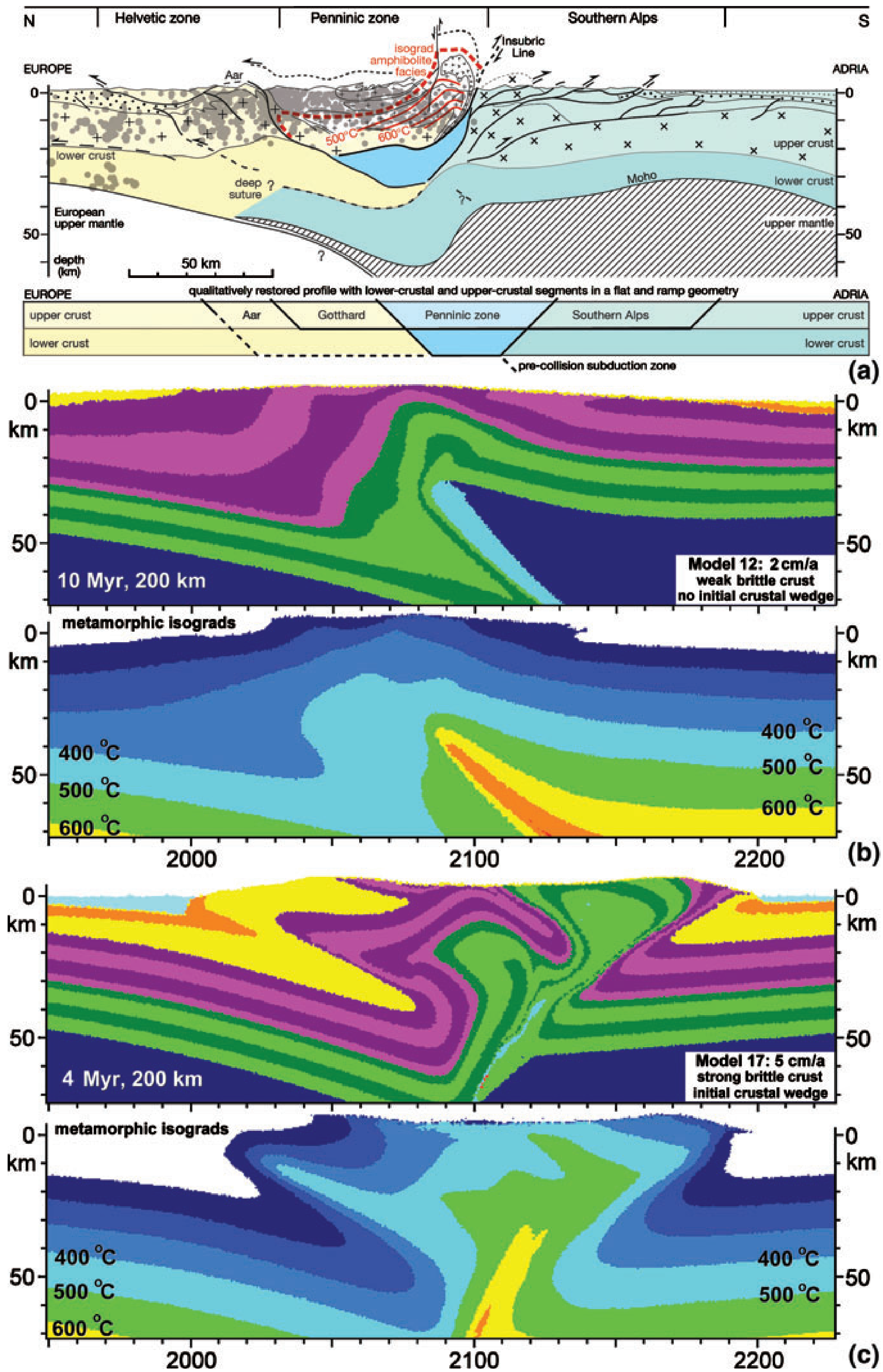

N
Helvetic zone
Penninic zone
Southern Alps
S
isograd amphibolite facies
Insubric Line
EUROPE
ADRIA
Aar
500°C
600°C
upper crust
lower crust
deep suture
Moho
lower crust
European upper mantle
upper mantle
depth (km)
50 km
EUROPE
qualitatively restored profile with lower-crustal and upper-crustal segments in a flat and ramp geometry
ADRIA
upper crust
Aar
Gotthard
Penninic zone
Southern Alps
upper crust
lower crust
lower crust
pre-collision subduction zone
(a)
10 Myr, 200 km
Model 12: 2 cm/a
weak brittle crust
no initial crustal wedge
metamorphic isograds
400 °C
500 °C
600 °C
2000
2100
2200
(b)
4 Myr, 200 km
Model 17: 5 cm/a
strong brittle crust
initial crustal wedge
metamorphic isograds
(c)

effective regional shear stresses τ_{xz} of 15–150 MPa, respectively (Fig. 2). The bulk deformation structure of numerical experiments with relatively strong lower crusts (Figs 7a,b & 13b,c) resemble the large-scale structure of the Central Alps (Fig. 13a) and suggest a significant role for strong viscous heating effects (Fig. 7e,f, Table 3). Granulites identified as the lower crust of Western Europe may constitute this strong rheological layer in the Alps (e.g. Schmid *et al.*, 1996). Additional numerical experiments with identical rheological setups but with a convergence rate of 5 cm a^{-1} confirm that 30–50 km wide positive temperature anomalies, as in the Lepontine Dome, are produced above the plate boundary, and maintained within the crust because of viscous heating (e.g. Figs 8i–l & 13c). In these models, viscous heating promotes upwelling of lower crustal rocks (cf. Fig. 8c,g), which adds to the positive temperature anomaly in the middle crust (Fig. 8k). Thermally induced buoyancy further amplifies this anomaly and crustal doming. This is further emphasized by Model 17 (Fig. 13c, Table 3), characterized by strong viscous heating ($\simeq 1.5\ \mu W\ m^{-3}$); its geometry and peak metamorphic temperature distribution after 200 km convergence show notably more similarity with the Lepontine Dome (Fig. 13a) than Model 12 (Fig. 13b, Table 2) characterized by low viscous heating ($\simeq 0.2\ \mu W\ m^{-3}$).

Although these numerical experiments are 2D, we speculate that thermally induced buoyancy in 3D will produce elongated dome-like structures in collision zones, such as the Lepontine Dome and the dome-shaped Tauern Window in the Alps (see also Stüwe, 1998). We attribute the fact that seismicity of the Central Alps is no deeper than *c.* 15 km (Fig. 13a), to ongoing viscous heating and subsequent rheological softening of the crust as a consequence of sustained collision.

CONCLUSION

Barrovian metamorphism is generally taken to have occurred because of increased radiogenic heating of a thickened crust (England & Thompson, 1984). This mechanism has been tested for the Lepontine Dome in the Central Alps but is not sufficiently consistent with geological information (Roselle & Engi, 2002). The numerical modelling developed here, using conservative estimates of parameters and variables, confirms that viscous heating is an alternative, *in situ* energy source associated with distributed deformation during continental collision. This mode of heat production may explain the closed shape of post-40 Ma isograds and may be sufficient to produce an additional 100–200 °C temperature increase in the Lepontine gneiss region. Many authors attributed the decompressional structural evolution of the Lepontine Dome to forced, upward extrusion assisted by efficient erosion of crustal units. Alternatively, our numerical modelling suggests that viscous heating has the potential to affect both temperature distribution and large-scale structural patterns within the deforming crust, notably accelerating exhumation of lower crustal rocks. Based on the similarities between models with strong lower crust and the geology of the central Alps, we conclude that the combination of viscous heating and moderate tectonic overpressure contribute to the heat/pressure budget of the Barrovian-type metamorphic field gradients inherent to any collisional orogens, without implying any external heat and pressure source.

ACKNOWLEDGEMENTS

This work was supported by ETH Research Grant TH -12/04-1, by RFBR grants nos 03-05-64633 and 1645-2003-5 to TVG and by the Deutsche Forschungsgemeinschaft within the scope of Sonderforschungsbereich 526 at Ruhr-University of Bochum. This work has benefited from constructive discussions with Y.Y. Podladchikov. We thank B. Kaus, D. Yuen, J. Connolly and A.B. Thompson for helpful comments and discussion on early versions of the manuscript. Special thanks are extended to S. Bodorkos and K. Stüwe, who provided much appreciated, thoughtful and thorough reviews. JMG editor R. Powell improved the clarity of our presentation.

REFERENCES

Allemand, P. & Lardeaux, J.-M., 1997. Strain partitioning and metamorphism in a deformable orogenic wedge: application to the Alpine belt. *Tectonophysics*, **280,** 157–169.

Babeyko, A. Y., Sobolev, S. V., Trumbull, R. B., Oncken, O. & Lavier, L. L., 2002. Numerical models of crustal scale convection and partial melting beneath the Altiplano-Puna plateau. *Earth and Planetary Science Letters*, **199,** 373–388.

Beaumont, C., Jamieson, R. A., Nguyen, M. H. & Lee, B., 2001. Himalayan tectonics explained by extrusion of a low-viscosity crustal channel coupled to focused surface denudation. *Nature*, **414,** 738–742.

Bittner, D. & Schmeling, H., 1995. Numerical modeling of melting processes and induced diapirism in the lower crust. *Geophysical Journal International*, **123,** 59–70.

Fig. 13. Comparison between (a) a geological profile across the Central Alps with deep structures from Burg *et al.* (2002) and dashed red lines showing the isotherms for peak metamorphic temperature in the Lepontine Dome from the maps of Steck & Hunziker (1994); Engi *et al.* (1995) and Todd & Engi (1997); dark circles are loci of seismic events after Deichmann *et al.* (2000), and (b) Model 12 and (c) Model 17 (Table 2). (b) and (c): same legend as Fig. 4. Same horizontal/vertical scales for (a)–(c). Model 17, which displays a cross sectional structure with crustal recumbent folding/imbrication that can be compared with the geological section involves more viscous heating than Model 12. Note the outward-dipping isograd pattern cutting the lithological boundaries in both models, as in the geological case. Blue-green boundary, crust–mantle boundary in models.

Brace, W. F. & Kohlstedt, D. T., 1980. Limits on lithospheric stress imposed by laboratory experiments. *Journal of Geophysical Research*, **85,** 6248–6252.

Brun, J.-P. & Cobbold, P. R., 1980. Strain heating and thermal softening in continental shear zones: a review. *Journal of Structural Geology*, **2,** 149–158.

Burg, J.-P., 1999. Ductile structures and instabilities: their implication for Variscan tectonics in the Ardennes. *Tectonophysics*, **309,** 1–25.

Burg, J.-P. & Laurent, P., 1978. Strain analysis of a shear-zone in a granodiorite. *Tectonophysics*, **47,** 15–42.

Burg, J.-P., Sokoutis, D. & Bonini, M., 2002. Model-inspired interpretation of seismic structures in the Central Alps: Crustal wedging and buckling at mature stage of collision. *Geology*, **30,** 643–646.

Burks, R. & Mosher, S., 1996. Multiple crenulation cleavages as kinematic and incremental strain indicators. *Journal of Structural Geology*, **18,** 625–642.

Burov, E., Jolivet, L., Le Pourhiet, L. & Poliakov, A., 2001. A thermomechanical model of exhumation of high pressure (HP) and ultra-high pressure (UHP) metamorphic rocks in Alpine-type collision belts. *Tectonophysics*, **342,** 113–136.

Chamberlain, C. P. & Sonder, L. J., 1990. Heat-producing elements and the thermal and baric patterns of metamorphic belts. *Science*, **250,** 763–769.

Clauser, C. & Huenges, E., 1995. Thermal conductivity of rocks and minerals. In: *Rock Physics and Phase Relations. AGU Reference Shelf 3*. (ed Ahrens, T.J.), pp. 105–126, American Geophysical Union, Washington, DC, USA.

Connolly, J. A. D. & Thompson, A. B., 1989. Fluid and enthalpy production during regional metamorphism. *Contributions to Mineralogy and Petrology*, **102,** 346–366.

Deichmann, N., Baer, M., Braunmiller, J. *et al*. 2000. Earthquakes in Switzerland and surrounding regions during 1999. *Eclogae Geologicae Helvetiae*, **93,** 395–406.

Dobretsov, N. L. & Kirdyashkin, A. G., 1992. Subduction zone dynamics: models of an accretionary wedge. *Ofioliti*, **17,** 155–164.

Doin, M.-P. & Henry, P., 2001. Subduction initiation and continental crust recycling: the roles of rheology and eclogitization. *Tectonophysics*, **342,** 163–191.

Dutruge, G. & Burg, J.-P., 1997. Strain localisation in an orthogneiss laccolith (the Pinet massif, Aveyron, southern France). *Tectonophysics*, **280,** 47–60.

Engi, M., Todd, C. S. & Schmatz, D. R., 1995. Tertiary metamorphic conditions in the eastern Lepontine Alps. *Schweizerische Mineralogische und Petrographische Mitteilungen*, **75,** 347–369.

Engi, M., Berger, A. & Roselle, G. T., 2001. Role of the tectonic accretion channel in collisional orogeny. *Geology*, **29,** 1143–1146.

England, P. C. & Thompson, A. B., 1984. Pressure–Temperature–time paths of regional metamorphism I. Heat transfer during the evolution of regions of thickened continental crust. *Journal of Petrology*, **25,** 894–928.

Escher, A. & Beaumont, C., 1997. Formation, burial and exhumation of basement nappes at crustal scale: a geometric model based on the Western Swiss–Italian Alps. *Journal of Structural Geology*, **19,** 955–974.

Frey, M. & Mählmann, R. F., 1999. Alpine metamorphism of the Central Alps. *Schweizerische Mineralogische und Petrographische Mitteilungen*, **79,** 135–154.

Gebauer, D., 1999. Alpine geochronology of the central and Western Alps: new constraints for a complex geodynamic evolution. *Schweizerische Mineralogische und Petrographische Mitteilungen*, **79,** 191–208.

Genser, J., van Wees, J. D., Cloetingh, S. & Neubauer, F., 1996. Eastern Alpine tectono-metamorphic evolution: constraints from two-dimensional *P–T–t* modelling. *Tectonics*, **15,** 584–604.

Gerya, T. V. & Stöckhert, B., 2002. Exhumation rates of high pressure metamorphic rocks in subduction channels: the effect of rheology. *Geophysical Research Letters*, **29,** article no. 1261 (April 15).

Gerya, T. V. & Yuen, D. A., 2003a. Characteristics-based marker-in-cell method with conservative finite-differences schemes for modeling geological flows with strongly variable transport properties. *Physics of the Earth and Planetary Interiors*, **140,** 295–320.

Gerya, T. V. & Yuen, D. A., 2003b. Rayleigh–Taylor instabilities from hydration and melting propel 'cold plumes' at subduction zones. *Earth and Planetary Science Letters*, **212,** 47–62.

Gerya, T. V., Stoeckhert, B. & Perchuk, A. L., 2002. Exhumation of high-pressure metamorphic rocks in a subduction channel: A numerical simulation. *Tectonics*, **21,** article no. 1056 (November–December).

Gerya, T. V., Yuen, D. A. & Maresch, W. V., 2004. Thermomechanical modelling of slab detachment. *Earth and Planetary Science Letters*, **226,** 101–116.

Goffé, B., Bousquet, R., Henry, P. & LePichon, X., 2003. Effect of the chemical composition of the crust on the metamorphic evolution of orogenic wedges. *Journal of Metamorphic Geology*, **21,** 123–141.

Graham, C. M. & England, P. C., 1976. Thermal regimes and regional metamorphism in the vicinity of overthrust faults: an example of shear heating and inverted metamorphic zonation from southern California. *Earth and Planetary Science Letters*, **31,** 142–152.

Grasemann, B. & Mancktelow, N. S., 1993. Two-dimensional thermal modelling of normal faulting: the Simplon fault zone, Central Alps, Switzerland. *Tectonophysics*, **225,** 155–165.

Grawinkel, A. & Stöckhert, B., 1997. Hydrostatic pore fluid pressure to 9 km depth – Fluid inclusion evidence from the KTB deep drill hole. *Geophysical Research Letters*, **24,** 3273–3276.

Grujic, D. & Mancktelow, N. S., 1996. Structure of the northern Maggia and Lebendun Nappes, Central Alps, Switzerland. *Eclogae Geologicae Helvetiae*, **89,** 461–504.

Hansen, U. & Yuen, D. A., 1996. Potential role played by viscous heating in thermal–chemical convection in the outer-core. *Geochimica et Cosmochimica Acta*, **60,** 1113–1123.

Hofmeister, A. M., 1999. Mantle values of thermal conductivity and the geotherm from phonon lifetimes. *Science*, **283,** 1699–1706.

Huenges, E., Erzinger, J., Kuck, J., Engeser, B. & Kessels, W., 1997. The permeable crust: Geohydraulic properties down to 9101 m depth. *Journal of Geophysical Research*, **102,** 18255–18265.

Huerta, A. D., Royden, L. & Hodges, K. V., 1998. The thermal structure of collisional orogens as a response to accretion, erosion, and radiogenic heating. *Journal of Geophysical Research*, **103,** 15287–15302.

Hunziker, J. C., Desmons, J. & Hurford, A. J., 1992. Thirty-two years of geochronological work in the Central and Western Alps: a review on seven maps. *Mémoires de Géologie (Lausanne)*, **13,** 1–59.

Jamieson, R. A., Beaumont, C., Fullsack, P. & Lee, B., 1998. Barrovian metamorphism: where's the heat? In: *What Drives Metamorphism and Metamorphic Reactions?* (eds Treloar, P.J. & O'Brien, P. J.), pp. 23–51. Geological Society Special Publication 138, London, UK.

Jamieson, R. A., Beaumont, C., Nguyen, M. H. & Lee, B., 2002. Interaction of metamorphism, deformation and exhumation in large convergent orogens. *Journal of Metamorphic Geology*, **20,** 9–24.

Kincaid, C. & Silver, P., 1996. The role of viscous dissipation in the orogenic process. *Earth and Planetary Science Letters*, **142,** 271–288.

Kukkonen, I. T. & Clauser, C., 1994. Simulation of heat transfer at the Kola deep-hole site – implications for advection, heat refraction and palaeoclimatic effects. *Geophysical Journal International*, **116,** 409–420.

Kusznir, N. J., 1991. The distribution of stress with depth in the lithosphere – Thermorheological and geodynamic constraints.

Philosophical Transactions of the Royal Society of London, **A337,** 95–110.

Landau, L. D. & Lifshitz, E. M., 1963. *Fluid Mechanics*. Pergamon Press, Oxford.

Laubscher, H., 1988. Material balance in Alpine orogeny. *Geological Society of America Bulletin*, **100,** 1313–1328.

Leloup, P. H., Ricard, Y., Battaglia, J. & Lacassin, R., 1999. Shear heating in continental strike-slip shear zones: model and field examples. *Geophysical Journal International*, **136,** 19–40.

Lippitsch, R., Kissling, E. & Ansorge, J., 2003. Upper mantle structure beneath the Alpine orogen from high-resolution teleseismic tomography. *Journal of Geophysical Research*, **108,** 2376 (DOI: 10.1029/2002JB002016).

Mancktelow, N. S., 1995. Nonlithostatic pressure during sediment subduction and the development and exhumation of high pressure metamorphic rocks. *Journal of Geophysical Research*, **100,** 571–583.

Marquer, D., Challandes, N. & Baudin, T., 1996. Shear zone patterns and strain distribution at the scale of a Penninic Nappe; the Suretta Nappe (Eastern Swiss Alps). *Journal of Structural Geology*, **18,** 753–764.

Merle, O., Cobbold, P. R. & Schmid, S., 1989. Tertiary kinematics in the Lepontine Dome. In: *Alpine Tectonics* (eds Coward, M.P., Dietrich, D. & Park, R.G.), pp. 113–134. Geological Society Special Publications 45, London, UK.

Miyashiro, A., 1973. *Metamorphism and Metamorphic Belts*. Wiley and Sons, New York, NY, USA.

Molnar, P. & England, P., 1990. Temperatures, heat flux and frictional stress near major thrust faults. *Journal of Geophysical Research*, **95,** B, 4833–4856.

Molnar, P. & Lyon-Caen, H., 1988. Some simple physical aspects of the support, structure and evolution of mountain belts. *Geological Society of America*, Special Paper, **218,** 179–207.

Nagel, T., De Capitani, C. & Frey, M., 2002. Isograds and *P–T* evolution in the eastern Lepontine Alps (Graubünden, Switzerland). *Journal of Metamorphic Geology*, **20,** 309–324.

Niggli, E., 1970. Alpine Metamorphose und Alpine Gebirgsbildung. *Fortschritte der Mineralogie*, **47,** 16–26.

Peacock, S. M., 1992. Blueschist-facies metamorphism, shear heating, and *P–T–t* paths in subduction shear zones. *Journal of Geophysical Research*, **97,** 17693–17707.

Petrini, K. & Podladchikov, Y., 2000. Lithospheric pressure–depth relationship in compressive regions of thickened crust. *Journal of Metamorphic Geology*, **18,** 67–77.

Pinkerton, H. & Stevenson, R. J., 1992. Methods of determining the rheological properties of magmas at subliquidus temperatures. *Journal of Volcanology and Geothermal Research*, **53,** 47–66.

Platt, J. P. & Behrmann, J. H., 1986. Structures and fabrics in a crustal-scale shear zone, Betic Cordillera, SE Spain. *Journal of Structural Geology*, **8,** 15–33.

Poirier, J.-P., Bouchez, J.-L. & Jonas, J.-J., 1979. A dynamic model for aseismic ductile shear zones. *Earth and Planetary Science Letters*, **43,** 441–453.

Pysklywec, R. N., Beaumont, C. & Fullsack, P., 2000. Modeling the behavior of the continental mantle lithosphere during plate convergence. *Geology*, **28,** 655–658.

Pysklywec, R. N., Beaumont, C. & Fullsack, P., 2002. Lithospheric deformation during the early stages of continental collision: numerical experiments and comparison with South Island, New Zealand. *Journal of Geophysical Research*, **107,** article no. 2133 (July).

Ramsay, J. G., 1967. *Folding and Fracturing of Rocks*. McGraw-Hill, New York, NY, USA.

Ramsay, J. G. & Graham, R. H., 1970. Strain variation in shear belts. *Canadian Journal of Earth Sciences*, **7,** 786–813.

Ramsay, J. G. & Huber, M. I., 1983. *The Techniques of Modern Structural Geology – Volume 1: Strain Analysis*. Academic Press, London, UK.

Ranalli, G., 1995. *Rheology of the Earth*. Chapman & Hall, London, UK.

Roselle, G. T. & Engi, M., 2002. Ultra high pressure (UHP) terrains: lessons from thermal modeling. *American Journal of Science*, **302,** 410–441.

Rütti, R., 2001. Tectono-metamorphic evolution of the Simano-Adula nappe boundary, Central Alps, Switzerland. *Schweizerische Mineralogische und Petrographische Mitteilungen*, **81,** 115–129.

Schlunegger, F., 1999. Controls of surface erosion on the evolution of the Alps: constraints from the stratigraphies of the adjacent foreland basins. *International Journal of Earth Sciences*, **88,** 285–304.

Schlunegger, F. & Willett, S., 1999. Spatial and temporal variations in exhumation of the central Swiss Alps and implications for exhumation mechanisms. In: *Exhumation Processes: Normal Faulting, Ductile Flow and Erosion* (eds Ring, U., Brandon, M. T., Lister, G. S. & Willett, S. D.), pp. 157–179, Geological Society Special Publications 154, London, UK.

Schmid, S. M., Pfiffner, O. A., Froitzheim, N., Schönborn, G. & Kissling, E., 1996. Geophysical–geological transect and tectonic evolution of the Swiss–Italian Alps. *Tectonics*, **15,** 1036–1064.

Schmidt, M. W. & Poli, S., 1998. Experimentally based water budgets for dehydrating slabs and consequences for arc magma generation. *Earth and Planetary Science Letters*, **163,** 361–379.

Scholz, C. H., 1980. Shear heating and the state of stress on faults. *Journal of Geophysical Research*, **85,** 6174–6184.

Schott, B., Yuen, D. A. & Schmeling, H., 2000. The significance of shear heating in continental delamination. *Physics of the Earth and Planetary Interiors*, **110,** 273–290.

Sibson, R. H., 1990. Faulting and fluid flow. In: *Fluids in Tectonically Active Regimes of the Continental Crust* (ed Nesbitt, B.E.), pp. 92–132, Mineralogical Association of Canada, Vancouver, BC, Canada.

Simpson, C., 1983. Displacement and strain patterns from naturally occurring shear zone terminations. *Journal of Structural Geology*, **5,** 497–506.

Spiegel, C., Kuhlemann, J., Dunkl, I., Frisch, W., von Eynatten, H. & Balogh, K., 2000. The erosion history of the Central Alps: evidence from zircon fission track data of the foreland basin sediments. *Terra Nova*, **12,** 163–170.

Steck, A. & Hunziker, J., 1994. The Tertiary structural and thermal evolution of the Central Alps – compressional and extensional structures in an orogenic belt. *Tectonophysics*, **238,** 229–254.

Stüwe, K., 1995. Thermal buffering effects at the solidus. Implications for the equilibration of partially melted metamorphic rocks. *Tectonophysics*, **248,** 39–51.

Stüwe, K., 1998. Heat sources of Cretaceous metamorphism in the Eastern Alps – a discussion. *Tectonophysics*, **287,** 251–269.

Stüwe, K., 2002. *Geodynamics of the Lithosphere*. Springer Verlag, Berlin, Germany.

Stüwe, K. & Sandiford, M., 1994. Contribution of deviatoric stresses to metamorphic *P–T* paths. An example appropriate to low-*P*, high-*T* metamorphism. *Journal of Metamorphic Geology*, **12,** 445–454.

Tenczer, V., Stüwe, K. & Barr, T. D., 2001. Pressure anomalies around cylindrical objects in simple shear. *Journal of Structural Geology*, **23,** 777–788.

Thompson, A. B. & Ridley, J. R., 1987. Pressure–temperature–time (*P–T–t*) histories of orogenic belts. *Philosophical Transactions of the Royal Society of London*, **A321,** 27–45.

Todd, C. S. & Engi, M., 1997. Metamorphic field gradients in the central Alps. *Journal of Metamorphic Geology*, **15,** 513–530.

Trommsdorff, V., 1966. Progressive Metamorphose kieseliger Karbonatgesteine in den Zentralalpen zwischen bernina und Simplon. *Schweizerische Mineralogische und Petrographische Mitteilungen*, **46,** 431–460.

Turcotte, D. L. & Schubert, G., 2002. *Geodynamics*. Cambridge University Press, Cambridge, UK.

Watts, M. J. & Williams, G. D., 1983. Strain geometry, microstructure and mineral chemistry in metagabbro shear zones: a

study of softening mechanisms during progressive mylonitization. *Journal of Structural Geology*, **5,** 507–517.
Wenk, E., 1956. Die lepontinische Gneissregion und die jungen Granite der Valle della Mera. *Eclogae Geologicae Helvetiae*, **49,** 251–265.
Winter, J. D., 2001. *An Introduction to Igneous and Metamorphic Petrology*. Prentice Hall, Upper Saddle River.
Yuen, D. A. & Schubert, G., 1981. Plateau uplifts as a consequence of frictional heating. *Tectonophysics*, **76,** 47–58.
Yuen, D. A., Balachandar, S. & Hansen, U., 2000. Modeling mantle convection: a significant challenge in geophysical fluid dynamics. In: *Geophysical and Astrophysical Convection* (eds Fox, P.A. & Kerr, R.M.), pp. 257–293, Gordon and Breach Science Publishers, Amsterdam, The Netherlands.

Received 24 June 2004; revision accepted 29 November 2004.

APPENDIX: INITIAL AND BOUNDARY CONDITIONS OF 2D MODELS

General setting

We employed the 2D finite difference code I2VIS with a marker-in-cell technique, which allows for the accurate solution of the governing equations on a rectangular fully staggered Eulerian grid for multiphase flow (Gerya & Yuen, 2003a). The 4000×670 km model (Fig. 3) is designed for the study of dynamic processes during continental collision involving subduction of the lithospheric mantle (e.g. Pysklywec *et al*., 2000). A non-uniform rectangular grid with a resolution varying from 2 to 30 km is used. It provides the highest resolution (2×2 km) in the upper central, 400 km wide and 100 km deep 'orogenic' area of the model (Fig. 3a). Continuous changes in the grid spacing are prescribed on 25 nodes with *c*. 12% grid step increment between adjacent nodes. The initial thermal structure of the colliding lithospheres with a 35-km thick crust corresponds to a steady temperature profile limited by the 1300 °C isotherm at 150 km depth. This implies a moderate thickness of continental mantle lithosphere and lower-crustal temperatures of 400–450 °C (Fig. 3a). At thicker mantle lithosphere, as in many continental sections, implies lower crustal temperatures and higher effective viscosity of crustal rocks, hence stronger viscous heating for the same convergence rate. Therefore, our results provide robust minimum estimates for the thermal effects of viscous heating during orogeny. The thermal boundary conditions are a 0 °C upper boundary and a zero horizontal heat flow across the vertical boundaries (Fig. 3b). An infinity-like *constant external temperature* condition along the bottom of the model implies 2045 °C at 1650 km depth, i.e. a constant temperature condition to be satisfied far below the lower boundary of the box, which allows both temperatures and vertical heat fluxes to vary along the permeable box lower boundary.

The velocity boundary conditions are free slip at all boundaries except the lower boundary of the box, which is permeable in both downward and upward directions (Fig. 3b). An infinity-like *external free slip* condition along the bottom of the model implies free slip at the 1650 km depth, i.e. free slip condition is satisfied far below the lower boundary of the box. In contrast to the model employed by Pysklywec *et al*. (2000) the source of motion is located within and not at a boundary of the computed region. For different numerical experiments, collision is prescribed either (1) by prescribing a constant convergence rate (v_x) or (2) by applying constant horizontal deviatoric stresses (σ_{xx}) within the *convergence condition domain* of the lithosphere (red square in Fig. 3b). In some experiments, this domain was implemented within the mantle lithosphere only to account for the actual degree of rheological coupling between mantle and crust. The convergence velocities/stresses within the crust are then calculated by solving governing equations that take into account rheological coupling between the crust and the mantle lithosphere. The dynamic viscosity structure (Fig. 3b) corresponds to the given temperature distribution (Fig. 3a), and characterizes the velocity field associated with the movement of the mantle lithosphere at the initiation of numerical experiments. The nucleation of the subduction/collision area is imposed by a 5–20-km thick and down to 160-km deep (below the bottom of the crust) initial zone of weakness (Fig. 3a) that has a wet olivine rheology in the mantle lithosphere having otherwise a dry olivine rheology (Ranalli, 1995). The inclination angle of this zone changes downwards from 10 to 45°, thus simulating the curvature of the subduction plane (inset, Fig. 3a). Our test numerical experiments have shown that the initial shape of the weak zone provides efficient decoupling between the two converging plates and favours subduction of the incoming mantle lithosphere under the collisional orogen.

Topography

Continental collision affects the topographic evolution of adjacent regions and the models include surface movements in a simplified way. The surface is calculated dynamically at each time-step as a free surface (e.g. Gerya & Yuen, 2003b). To account for the topographic changes, we have implemented a low viscosity (10^{16} Pa s), initially 10-km thick layer above the upper continental crust (Fig. 3a). Its density is either 1 kg m^{-3} (air, above the $z = 10$ km sea level, with $z = 0 =$ top of the box) or 1000 kg m^{-3} (sea water, below the $z = 10$ km sea level). The interface between this very weak layer and the top of the continental crust is treated as an erosion/sedimentation surface, which evolves according to the transport equation solved in Eulerian coordinates at each time-step (Gerya & Yuen, 2003b):

$$\frac{\partial z_{\mathrm{es}}}{\partial t} = v_z - v_x \frac{\partial z_{\mathrm{es}}}{\partial x} - v_{\mathrm{s}} + v_{\mathrm{e}}, \tag{9}$$

where z_{es} is the vertical position of the surface as a function of the horizontal distance x; v_z and v_x are the vertical and horizontal components of the material velocity vector at the surface; $v_{\mathrm{s}}$and v_{e} are, sedimentation and erosion rates, respectively, which correspond to the relation:

$$v_{\mathrm{s}} = 0, v_{\mathrm{e}} = v_{\mathrm{e0}} \quad \text{when} \ \ z < 10\,\text{km},$$

$$v_{\mathrm{s}} = v_{\mathrm{s0}}, v_{\mathrm{e}} = 0 \quad \text{when} \ \ z \geq 10\,\text{km},$$

where v_{e0} and v_{s0} are imposed constant erosion and sedimentation rates, respectively.

Partial melting

Partial melting of the crust is an important metamorphic process during orogeny. Therefore, the numerical models allowed melting of the continental crust in the *P-T* region between the wet solidus and dry liquidus of crustal rocks (Gerya & Yuen, 2003b). As a first approximation, the volumetric fraction of melt M is assumed to increase linearly with temperature according to the relations:

$$M = 0 \quad \text{at} \ \ T \leq T_{\mathrm{solidus}}, \tag{10a}$$

$$M = \frac{(T - T_{\mathrm{solidus}})}{\left(T_{\mathrm{liquidus}} - T_{\mathrm{solidus}}\right)} \quad \text{at} \ \ T_{\mathrm{solidus}} < T < T_{\mathrm{liqidus}}, \tag{10b}$$

$$M = 1 \quad \text{at} \ \ T \geq T_{\mathrm{liquidus}}, \tag{10c}$$

whereT_{solidus} and T_{liquidus} are the wet solidus and dry liquidus temperatures of the crust, respectively (see Table 2 for definitions).

The effective density, ρ_{eff}, of partially molten rocks is calculated from:

$$\rho_{\mathrm{eff}} = \rho_{\mathrm{solid}} - M(\rho_{\mathrm{solid}} - \rho_{\mathrm{molten}}) \tag{11}$$

where ρ_{solid} and ρ_{molten} are the densities of solid and molten rock, respectively, which vary with pressure and temperature according to the relation:

$$\rho_{P,T} = \rho_0[1 - \alpha(T - T_0)][1 + \beta(P - P_0)], \tag{12}$$

where ρ_0 is the standard density at $P_0 = 0.1$ MPa and $T_0 = 298$ K; α and β are the thermal expansion and compressibility coefficients, respectively (Table 1).

The effect of latent heat (e.g. Stüwe, 1995) is included by increasing the effective heat capacity ($C_{p_{eff}}$) and thermal expansion (α_{eff}) of the partially molten rocks ($0 < M < 1$), calculated as

$$C_{p_{eff}} = C_p + Q_L\left(\frac{\partial M}{\partial T}\right)_P, \tag{13a}$$

$$\alpha_{eff} = \alpha + \rho\frac{Q_L}{T}\left(\frac{\partial M}{\partial P}\right)_T, \tag{13b}$$

where C_p is the heat capacity of the solid crust, and Q_L is the latent heat of melting of the crust (Table 2).

Rheological model

Viscosity dependent on strain rate, pressure and temperature is defined in terms of deformation invariants (Ranalli, 1995) as:

$$\eta_{creep} = (\dot{\varepsilon}_{II})^{(1-n)/2n}F(A_D)^{-1/n}\exp\left(\frac{E+V}{nRT}\right) \tag{14}$$

where $\dot{\varepsilon}_{II} = 1/2\dot{\varepsilon}_{ij}\dot{\varepsilon}_{ij}$ is the second invariant of the strain rate tensor and A_D, E, V and n are experimentally determined flow law parameters (Tables 1 & 2). F is a dimensionless coefficient depending on the type of experiments on which the flow law is based. For example:

$$F = \frac{2^{(1-n)/n}}{3^{(1+n)/2n}} \quad \text{for triaxial compression and}$$

$$F = 2^{(1-2n)/n} \quad \text{for simple shear.}$$

For rocks containing relatively small melt fractions, ($M < 0.1$), the ductile rheology is combined with a brittle rheology to yield an effective viscoplastic rheology. For this purpose the Mohr-Coulomb yield criterion (e.g. Ranalli, 1995) is implemented by limiting creep viscosity, η_{creep}, as follows:

$$\eta_{creep} \le \frac{(N_1P + N_2)(1-\lambda)}{(4\dot{\varepsilon}_{II})^{1/2}}, \tag{15}$$

where P is dynamic (non-lithostatic) pressure, N_1 and N_2 are empirical constants (Brace & Kohlstedt, 1980). The pore fluid pressure λ (Table 1) controls the brittle strength of fluid-containing porous or fractured media. A hydrostatic gradient with a pore pressure coefficient $\lambda = 0.4$ is generally accepted for the upper crust (e.g. Sibson, 1990). Hydrocarbon exploration wells have shown that in sedimentary basins the transition from a hydrostatic to a near-lithostatic pore pressure gradient generally occurs at *c.* 3–5 km depth (e.g. Sibson, 1990). However, the KTB and Kola boreholes have shown that a hydrostatic pore pressure gradient can reach down to more then 9 km depth and a temperature of 265 °C (Kukkonen & Clauser, 1994; Grawinkel & Stöckhert, 1997; Huenges *et al.*, 1997). For simplicity, we assumed a continuous transition from the hydrostatic pore fluid pressure ($\lambda = 0.4$) at the surface to a characteristic pore fluid pressure ($\lambda_{10} = 0.5$–0.9) at 10 km depth. Intermediate pore fluid pressures are thus assumed at shallow depths <10 km, with an effective pore fluid pressure calculated as follows (Gerya *et al.*, 2002):

$$\begin{aligned} \lambda &= \frac{0.4(10-\Delta z_{es}) + \lambda_{10}\Delta z_{es}}{10} \quad \text{when} \quad 0 \le \Delta z_{es} \le 10\,\text{km} \\ \lambda &= \lambda_{10} \quad \text{when} \quad \Delta z_{es} > 10\,\text{km}, \end{aligned} \tag{16}$$

where Δz_{es} is the depth beneath the calculated dynamic erosion/sedimentation surface in km. The brittle strength of the mantle is assumed to be high because of the absence of free pore fluid [$\lambda_{10} = 0$ in Eq. (16)].

The effective viscosity η of molten rocks ($M > 0.1$) was calculated by using the formula (Pinkerton & Stevenson, 1992; Bittner & Schmeling, 1995):

$$\eta = \eta_0\exp\left[2.5 + (1-M)\left(\frac{1-M}{M}\right)^{0.48}\right] \tag{17}$$

where η_0 is an empirical parameter depending on rock composition, $\eta_0 = 10^{13}$ Pa s is taken for molten mafic rocks (i.e. $1 \times 10^{14} \le \eta \le 2 \times 10^{15}$ Pa s for $0.1 \le M \le 1$) and $\eta_0 = 5 \times 10^{14}$ Pa s (i.e. $6 \times 10^{15} \le \eta \le 8 \times 10^{16}$ Pa s for $0.1 \le M \le 1$) for felsic rocks (Bittner & Schmeling, 1995). 10^{16} and 10^{26} Pa s are the lower and upper cut values for viscosity of all types of rocks in our numerical experiments.

Conservation equations and numerical implementation

We have considered 2D creeping flow wherein both thermal and chemical buoyant forces are included along with heating from adiabatic compression and viscous dissipation in the heat conservation equation.

We have adopted (Gerya & Yuen, 2003a) a Lagrangian frame in which the heat conservation equation with a thermal conductivity $k(T, P, C)$ (Table 2) dependent on rock composition (C), pressure and temperature (e.g. Hofmeister, 1999)) that takes the form:

$$\rho C_p\left(\frac{DT}{Dt}\right) = -\frac{\partial q_x}{\partial x} - \frac{\partial q_z}{\partial z} + H_r + H_a + H_S \tag{18}$$

in which

$$q_x = -k(T,P,C)\frac{\partial T}{\partial x}, q_z = -k(T,P,C)\frac{\partial T}{\partial z},$$

$$H_a = T\alpha\left(v_x\frac{\partial P}{\partial x} + v_z\frac{\partial P}{\partial z}\right), H_S = \sigma_{xx}\dot{\varepsilon}_{xx} + \sigma_{zz}\dot{\varepsilon}_{zz} + 2\sigma_{xz}\dot{\varepsilon}_{xz},$$

where D/Dt represents the substantive time derivative, H_r is the radioactive heating which depends on advected rock composition (Table 2) and other notations are shown in Table 1. We emphasize the presence of the viscous heat production term H_S in the temperature equation because it plausibly has significant but understudied effect on the collisions process.

The conservation of mass is approximated by the incompressible mass conservation (continuity) equation.

$$\frac{\partial v_x}{\partial x} + \frac{\partial v_z}{\partial z} = 0. \tag{19}$$

The 2D Stokes equations for creeping flow take the form:

$$\frac{\partial \sigma_{xx}}{\partial x} + \frac{\partial \sigma_{xz}}{\partial z} = \frac{\partial P}{\partial x} \tag{20}$$

$$\frac{\partial \sigma_{zz}}{\partial z} + \frac{\partial \sigma_{xz}}{\partial x} = \frac{\partial P}{\partial z} - g\rho(T,P,C,M) \tag{21}$$

The density $\rho(T, P, C, M)$ depends explicitly on temperature, pressure, rock composition and melt fraction.

We employ viscous constitutive relationships between stress and strain-rate with η representing the effective viscosity, which depends on composition, temperature, pressure, strain-rate and melt fraction:

$$\sigma_{ij} = 2\eta\dot{\varepsilon}_{ij}. \tag{22}$$

It is also worth noting that dynamic (and not depth-dependent lithostatic) pressure was consistently used in all calculations including rheological and melting models, thus taking into account effects of non-lithostatic pressures in compressive regions of thickened crust (Petrini & Podladchikov, 2000).